Histone H2A ubiquitination resulting from Brap loss of function connects multiple aging hallmarks and accelerates neurodegeneration

Yan Guo[1], Alison A. Chomiak[1], Ye Hong[2], Clara C. Lowe[3], Wen-Ching Chan[4], Jorge Andrade[4,&], Hongna Pan[3], Xiaoming Zhou[5], Eugene Berezovski[3], Edwin S. Monuki[6], and Yuanyi Feng[1,3*]

1. Department of Neurology, Northwestern University Feinberg School of Medicine, 303 E. Superior Street, Chicago, IL 60611, U.S.A

2. University of Turku, 20500 Turku, Finland

3. Department of Biochemistry and Molecular Biology, Uniformed Services University, 4301 Jones Bridge Road, Bethesda, MD 20814, U.S.A

4. Center for Research Informatics, University of Chicago, Chicago, IL, U.S.A

5. Department of Medicine, Uniformed Services University, 4301 Jones Bridge Road, Bethesda, MD 20814, U.S.A

6. Department of Pathology & Laboratory Medicine, University of California, Irvine, Irvine, CA, U.S.A

& Present address: Kite Pharma, Santa Monica, CA 90404, U.S.A

*To whom correspondence should be addressed:

Tel: (301) 295-9419

Email: yuanyi.feng@usuhs.edu

SUMMARY

Aging is an intricate process that is characterized by multiple hallmarks including stem cell exhaustion, genome instability, epigenome alteration, impaired proteostasis, and cellular senescence. While each of these is detrimental at the cellular level, it remains unclear how they are interconnected to cause systemic organ deterioration. Here we show that abrogating Brap, a BRCA1 associated protein, results in cellular senescence with persistent DNA double-strand breaks and elevation of histone H2A mono- and poly-ubiquitination (H2Aub). The high H2Aub initiates proteasome-dependent histone proteolysis, leading to global epigenetic alteration, ubiquitinated protein accumulation, and senescence reinforcement. When these defects occur in mice carrying Brap deletions in cerebral cortical neural progenitors or postnatal neurons, they accelerate brain aging, induce neurodegeneration, and shorten lifespan. As we show H2Aub is also increased in human brain tissues of Alzheimer's disease, these data together suggest that chromatin aberrations mediated by H2Aub act as a nexus of multiple aging hallmarks.

INTRODUCTION

Aging is a natural process that connects birth and death. The time-dependent decline in organ function during aging is the major risk factor for developing many diseases including neurodegenerative disorders (NDs). Yet, the etiology of aging is complex and multifactorial. It is associated with several cellular and molecular hallmarks, such as stem cell exhaustion, genome instability, epigenetic alteration, deregulated nutrient sensing, mitochondrial dysfunction, cellular senescence, and loss of proteostasis (Lopez-Otin et al., 2013). For neurodegeneration, additional hallmark defects in neuronal calcium homeostasis and neuronetwork activity, as well as increased glial cell activation and neuroinflammation are also essential contributors to the physical and functional deterioration of the brain (Mattson and Arumugam, 2018). Aging at the organismal or system level does not simply result from the dysfunction of any individual cellular or molecular process or a linear pathway. To cause progressive and irreversible organ-wide degeneration, multiple aging promoting factors must act in concert. However, the mechanism underlying interconnections among various aging hallmarks is poorly understood, forming a major barrier to combating aging-associated diseases.

Among various aging hallmarks, genome instability poses a lifelong threat to all living cells and can result in increased somatic mutations that have been shown to accumulate with age in most organs (Lombard et al., 2005; Soares et al., 2014; White and Vijg, 2016). Besides a clear link to carcinogenesis, loss of genome stability has also been implicated in neurodegeneration (Bushman et al., 2015; Madabhushi et al., 2014; Mitra et al., 2019; Rulten and Caldecott, 2013; Shanbhag et al., 2019; Thadathil et al., 2019), and there has been long-established evidence for significant levels of DNA damage in non-dividing cells, such as neurons in the brain (Lodato et al., 2015; Lu et al., 2004; Rutten et al., 2007; Suberbielle et al., 2013). Recent whole genome

sequencing analyses have further demonstrated that somatic mutations increase with age in both bulk tissues and single neurons of the human brain (Hoang et al., 2016; Lodato et al., 2018). Moreover, mutations of genes important for genome maintenance and DNA repair cause progeroid syndromes and often manifest with both premature aging and neurodegeneration (Choy and Watters, 2018; Coppede and Migliore, 2010; Kakigi et al., 1992; Weidenheim et al., 2009). Thus, genotoxicity is a universal insult that not only is concomitant with old age but also drives aging-associated diseases. Nevertheless, the mechanism by which neuronal DNA damage causes brain aging and neurodegeneration at the system level remains elusive.

A plausible mechanism for DNA damage to induce tissue-wide degeneration is via cellular senescence, a stress response that occurs when cells experience telomere erosion, chronic oncogenic stimulation, persistent DNA damage, oxidative and metabolic stresses, or mitochondrial dysfunction (Hayflick, 1965; Hernandez-Segura et al., 2018; McHugh and Gil, 2018; Munoz-Espin and Serrano, 2014; Rodier and Campisi, 2011). Although originally defined by a permanent replication arrest, cellular senescence is also characterized by a set of distinctive phenotypes, including expression of a cyclin-dependent kinase inhibitor (CKI) $p16^{Ink4a}$, activation of senescence-associated β-galactosidase (SA-β-gal), alterations of global epigenetic and metabolic profiles, resistance to apoptosis, increases in autophagy, and implementation of a complex and multicomponent secretome known as the senescence-associated secretory phenotypes (SASP) (Campisi and Robert, 2014; Coppe et al., 2008; Munoz-Espin and Serrano, 2014; Rodier and Campisi, 2011). Through SASP, senescent cells produce a myriad of pro-inflammatory cytokines, chemokines, growth factors, and proteases (Kuilman and Peeper, 2009; Lasry and Ben-Neriah, 2015). These secreted molecules act through autocrine signaling to reinforce the senescence state and, through paracrine signaling, to affect neighboring cells.

However, it remains to be experimentally tested whether neurons, which are replication-incompetent by nature, can acquire the additional characteristics of senescent cells upon chronic DNA damage to promote neuroinflammation and neurodegeneration.

We have been studying the impact of genome instability on cerebral cortical neurogenesis, during which we identified Brap as a key player through its interaction with essential genes for human brain development and brain genome protection (Houlihan and Feng, 2014; Lanctot et al., 2013). BRAP/Brap is a ubiquitously expressed cytoplasmic protein originally cloned through its interaction with the BRCA1 tumor suppressor (Li et al., 1998). It was also found to act as a ubiquitin E3 ligase and an effector of activated RAS (Matheny et al., 2004). Our study of Brap in central nervous system neurogenesis has demonstrated that it is a multifaceted molecule and can modulate the mode of signaling propagation downstream of RAS in a context-dependent fashion (Lanctot et al., 2013). Additionally, the E3 ligase activity of Brap allows it to serve as a liaison between the cell's environment and cell nucleus by targeting other E3 ligases with a wide-range of nuclear substrates (Lanctot et al., 2017). Moreover, the essential role of Brap goes beyond development. In a recent genome-wide association study of 500,000 genotyped individuals along with information on their parents' age and cause of death, the *BRAP* gene locus was linked to the human lifespan (Timmers et al., 2019). This has suggested a functional contribution of BRAP to human aging.

By analyzing Brap null ($Brap^{-/-}$) and cerebral cortical neural progenitor cell (NPC) conditional Brap knockout ($Brap^{cKONPC}$) mice, we have shown that Brap loss of function (LOF) skews the cell cycle kinetics of multipotent NPCs, resulting in abrogation of the G1/S checkpoint and impeded generation of cerebral cortical neurons (Lanctot et al., 2017). We now demonstrate that besides the functional exhaustion of neural stem/progenitor cells, $Brap^{cKONPC}$ mice also

present persistent DNA double-strand breaks (DSBs), increased cellular senescence, and significantly decreased life expectancy. The accelerated aging of Brap^{cKONPC} mice is accompanied by neuroinflammatory and neurodegenerative phenotypes along with remarkable cerebral cortical proteinopathy. DSBs in cortical neurons of Brap^{cKONPC} mice elevate Brca1 as well as the level of histone H2A ubiquitination (H2Aub), which is known to be targeted by the Brca1 E3 ligase activity. We show that the high H2Aub resulting from Brap LOF can target histones for proteolysis, leading to global chromatin structural changes, a backlog of ubiquitinated proteasome substrates, and senescence reinforcement. These data collectively suggest that histone H2Aub, as a mediator of genome instability and epigenetic alteration, is a key node connecting multiple aging hallmarks. As we also demonstrate that H2Aub is elevated in cortical tissue from patients with Alzheimer's disease (AD), the results of this study highlight an essential impact of chromatin aberrations on aging and NDs.

RESULTS

Brap LOF results in accelerated cellular senescence with persistent DSBs

To further query the skewed cell cycle kinetics and impeded differentiation of Brap- deficient NPCs that we observed previously, we isolated NPCs from Brap$^{-/-}$ embryos (before embryonic lethality by E13.5) and studied them in culture as neurospheres. Consistent with our previous finding of an unaltered number of NPCs in Brap$^{-/-}$ and Brap^{cKONPC} embryos, Brap$^{-/-}$ NPCs grew at a rate comparable to their wild-type (WT) counterparts in the first 4-5 days *in vitro* (div) but abruptly ceased proliferation after 7-8 days (Figure 1A). This growth arrest was neither reverted by altering the concentration and component of growth factors in the culture media nor

accompanied by increased apoptosis (Figure 1B). We thus suspected that the mutant NPCs reached their replicative lifespan due to cellular senescence.

To determine if Brap LOF indeed results in cellular senescence, we turned to mouse embryonic fibroblast (MEFs) as they are better established for senescence analyses. We isolated MEFs from Brap$^{-/-}$ and WT embryos and cultured them following the 3T3 cell protocol (Todaro and Green, 1963). As expected, a greater fraction of Brap$^{-/-}$ MEFs showed multiple essential characteristics of cellular senescence as early as passage 2 (P2). These include an enlarged cell body, high senescence-associated beta-galactosidase (SA-β−gal) activity, and loss of the Ki67 proliferation marker (Figure 1C, D). The expression of the p16^{Ink4a} CKI is a common indicator of cellular senescence. As an antibody to murine p16^{Ink4a} is unavailable, we examined p19^{Arf}, a CKI encoded by the p16^{Ink4a} locus but alternatively transcribed and can act together with p16^{Ink4a} to induce cellular senescence (Capparelli et al., 2012; Haber, 1997; Quelle et al., 1995). We found that the elevation of p19^{Arf} was readily detectable in Brap$^{-/-}$ MEFs as early as P1, while increases in canonical G1/S CKIs, such as p27^{Kip1} and p21^{Cip1}, were inconsistent and insignificant presumably due to Skp2-mediated degradation as shown in Brap$^{-/-}$ NPCs and embryos(Lanctot et al., 2017) (Figure 1 E, F). We further validated the senescence phenotype of Brap LOF by examining the loss of Lamin B1, another characteristic of cellular senescence (Freund et al., 2010). Both immunofluorescence (IF) and immunoblotting (IB) analyses demonstrated that Lamin B1 was downregulated much more rapidly in Brap$^{-/-}$ than WT MEFs from P1 to P3 (Figure 1G, H). To acquire the ultimate proof that cellular senescence is the consequence of Brap LOF, we assessed several known SASP molecules, including Mmp1, Mmp2, Serpin1 (Pai1), and Osteopontin/Spp1 (OPN) (Aoshiba et al., 2013; Castello et al., 2017; Coppe et al., 2010; Flanagan et al., 2018; Ghosh and Capell, 2016; Pazolli et al., 2012; Rao and Jackson, 2016;

Vaughan et al., 2017). We found that all of them were elevated and/or activated in Brap$^{-/-}$ MEFs along with increased phosphorylation of NFkB p65^{S536}, a chief mediator for SASP(Salminen et al., 2012) (Figure 1I). The occurrence of multiple essential features of senescent cells demonstrates unambiguously that Brap LOF leads to accelerated cellular senescence. These data also suggest that the reduced stemness of NPCs in the embryonic cerebral cortex of Brap$^{-/-}$ and Brap^{cKONPC} mice was caused by a pro-senescence change.

Next, we found that the accelerated cellular senescence caused by Brap LOF was associated with strong and persistent DNA damage responses (DDRs), a major mechanism for senescence induction (d'Adda di Fagagna, 2008; McHugh and Gil, 2018; White and Vijg, 2016). Significant elevations of phospho-p53, -Atm, -Atr, and 53BP1 were detected in Brap$^{-/-}$ MEFs as early as in P1 (Figure 2A-C). By P3, a large fraction of Brap$^{-/-}$ MEFs showed persistent DNA damage foci with high levels of γH2A.X, the hallmark of DNA double-strand breaks (DSBs), and 53BP1, a marker for DSBs repair (Panier and Boulton, 2014; Thiriet and Hayes, 2005)(Figure 2D-F). Notably, the large γH2A.X and 53BP1 foci were in both proliferating (Ki67+) cells and cells that had ceased dividing (Ki67-) (Figure 2D, E, high magnification panels), indicating that DSBs in Brap$^{-/-}$ MEFs were intractable and persisted into cells that had undergone replication arrest. Furthermore, when histone extracts were analyzed by IB, we found γH2A.X was not only significantly elevated but also became predominantly ubiquitinated in Brap$^{-/-}$ MEFs coinciding with their rapid progression to senescence (Figure 2F). The ubiquitinated moiety of γH2A.X was shown to be a specific biomarker for non-apoptotic DSBs and could be induced by oxidative DNA damage (Luczak and Zhitkovich, 2018). This agrees with the lack of apoptosis of Brap$^{-/-}$ cells and the observation of the enhanced ubiquityl-γH2A.X with H_2O_2 treatment (Figure 2F). Therefore, the high level of γH2A.X ubiquitination is a unique

phenotype of Brap LOF, which underlies its apoptosis-resistant and senescence-prone cell fate in response to DSBs.

Elevated cellular senescence and DSBs in cerebral cortical tissue underlie shortened lifespan of Brap^{cKONPC} mice

The accelerated cellular senescence and persistent DSBs shown by Brap$^{-/-}$ cells in culture prompted us to further ask whether similar defects occur *in vivo* in Brap mutant mice. We thus looked into brain phenotypes of the adult Brap^{flox} Emx1-Cre mice (referred to as Brap^{cKONPC}), in which the expression of Cre recombinase in NPCs of the dorsal telencephalon abrogates Brap in glutamatergic neurons, astroglia, and oligodendrocytes of the cerebral cortex (Gorski et al., 2002). We followed a cohort of Brap^{cKONPC} mice (n= 46) and their Brap$^{flox/WT}$ or Brap$^{flox/flox}$ Cre-control littermates (n=29) over 12 months. We found that most Brap^{cKONPC} mice die between 4 and 8 months with a median lifespan of 6 months (Figure 2G). The mutant mice lost weight, became lethargic, and showed slow or labored breathing when death became imminent (Supplementary Video). Since Brap's absence was limited to the cortical tissue in Brap^{cKONPC} mice, these findings show that cerebral cortex deterioration can result in accelerated aging and midlife mortality.

We next found that the premature death of Brap^{cKONPC} mice was associated with increased cellular senescence in cerebral cortical tissue. First, higher SA-β-gal activity was shown by many mutant cortical cells with the morphology of pyramidal neurons (Figure 2H, arrows). This suggested that, despite being replication-incompetent, neurons can undergo additional senescence-associated chromatin and metabolic changes due to Brap LOF. To further examine increased cellular senescence, we assessed the expression of p16^{Ink4} by qRT-PCR and

found it was significantly elevated in Brap^{cKONPC} over control cortices (Figure 2I). In addition, we showed that the level of Lamin B1 was decreased in the cortical tissue of Brap^{cKONPC} mice along with increased SASP factors including Serpin1 (Pai-1), Mmp2, Ssp1 (OPN), and phospho-NFkB (Figure 2J). Together, these data demonstrate that increased cellular senescence is also a phenotype of Brap LOF in the cerebral cortical tissue.

Similar to our observations in MEFs, we found that the cellular senescence in Brap^{cKONPC} cortices was associated with persistent DSBs and increased γH2A.X ubiquitination. To evaluate DSBs in Brap^{cKONPC} mice, we first analyzed histone extracts from the cortical tissues of adult Brap^{cKONPC} and control mice by IB. We found that γH2A.X in the Brap^{cKONPC} cortices was not only elevated but also mono- and poly-ubiquitinated, showing a dominant pool of approximately 60 kDa that is equivalent to the molecular weight of γH2A.X with Penta-ubiquitin conjugations (Figure 2K). Correlated with increased γH2A.X, 53BP1 was found at higher levels in Brap^{cKONPC} than in control cortical tissues at all postnatal ages, indicating that DSBs in the mutant cortex were persistent (Figure 2L). We next sought to identify the cell type of DSBs in Brap^{cKONPC} cortices by immunohistological (IH) analyses. We found γH2A.X was present in the nucleus of a substantial fraction of mutant cortical neurons (NeuN+) but was neither in mutant glia (NeuN-) nor in the cortices of WT mice (Figure 2M). Given that neurons cannot replicate and that we did not observe brain tumors or elevated apoptosis in the Brap^{cKONPC} brain (Figure 2N), our finding suggests that senescence is the major consequence of chronic neuronal DSBs and underlies the shortened lifespan.

Transcriptomic profiles of Brap^{cKONPC} cortices reveal SASP candidates, immune activation, and impaired synaptic signaling

Compared to apoptosis, senescence following unsuccessful DSB repair is more deleterious at the system level, as senescent cells are stably viable and can chronically influence neighboring cells by secreting soluble molecules or by altering cell surface and extracellular matrix (ECM) proteins. We thus sought to explore the SASP profiles associated with neuronal DSBs by identifying molecules that significantly gain expression in Brap^{cKONPC} cortices. RNA sequencing (RNA-seq) was carried out with cerebral cortical total transcripts of Brap^{cKONPC} and littermate control mice of 3 months old, the age when high levels of cellular senescence were observed in Brap^{cKONPC} cortical tissues. We identified 811 differentially expressed genes (DEGs) between the Brap^{cKONPC} and the control group (n=5 in each group), and 373 genes were significantly upregulated by Brap LOF (Figure 3A, Supplemental Table 1). Consistent with the pro-inflammatory feature of cellular senescence, we found 67 of the upregulated genes encode molecules associated with cells of the immune system and/or regulators of the innate immune response (Figure 3B). The upregulation of these genes reflects inflammatory pathology in the mutant brain tissue. Moreover, 80 upregulated genes encode secreted molecules, which represent the cerebral cortical secretome of Brap^{cKONPC} mice. Increased expression of these molecules can pose non-cell autonomous effects via SASP. These SASP candidate genes include not only immune active molecules and proteases but also diverse neuropeptide neurotransmitters and peptide hormones with potent activities in neural networking and cerebrovascular regulation (Figure 3C). An additional 83 upregulated genes encode plasma membrane and ECM proteins that interphase cells with their environment (Figure 3D). Increased expression of these genes can alter intercellular communication and tissue homeostasis. The most significantly upregulated genes in Brapc^{KONPC} cortices also include regulators for neurotransmitter metabolism, fatty acid and cholesterol metabolism, protein synthesis and sorting, as well as calcium homeostasis

(Figure 3A, Supplemental Table 1). These gained activities can dominantly affect multiple cell types, resulting in brain-wide alterations in innate immunity and neural function.

Brap LOF also resulted in decreased expression of 438 genes in the cortical tissue (Supplemental Table 1). Notably, the most significant downregulation occurred in genes that play key roles in regulating energy homeostasis, neuronal activity, synaptic plasticity, neuronal excitatory-inhibitory balance, Wnt signaling, retinoid metabolism, as well as the production, secretion, and activity control of neuropeptides or neurotransmitters (Figure 3A). We performed Gene Ontology (GO) enrichment analysis of the 50 most significantly downregulated genes in $Brap^{cKONPC}$ cortices. The GO terms identified in the BP category include impaired biological functions mainly in synaptic transmission as well as in cellular responses to stimuli and neuronal morphogenesis (Figure 3E). These data suggest that neuronal DSBs and increased cellular senescence not only induce neuroinflammation but also cause marked neural dysfunction that underpins the accelerated brain aging of $Brap^{cKONPC}$ mice.

Enhanced neuroinflammation and neurodegeneration in $Brap^{cKO}$ brain

As neuroinflammation is not only a common feature of senescence and tissue aging but also a key contributor to neurodegeneration, the gained expression of immune-responsive genes and downregulation of essential genes for neurofunction in $Brap^{cKONPC}$ cortices suggested strongly that DSBs and cellular senescence caused neurodegeneration. Therefore, we examined neuroinflammatory and neurodegenerative phenotypes and found they were readily detectable in $Brap^{cKONPC}$ cortices starting at 3 months and progressing rapidly with age.

First, hyperphosphorylation of the microtubule-associated protein tau became significantly increased in the cortical tissue of $Brap^{cKONPC}$ mice at 3 months and was further

elevated as the mutant mice grew older (Figure 4A, B). Increased tau phosphorylation in Brap^{cKONPC} cortices was found on multiple residues including T181, T217, S396, and S416 (Figure 4A). The hyperphosphorylation on these residues is known to be associated with insoluble tau aggregates and neurodegenerative diseases. As the presence of these human tauopathy-like changes in Brap^{cKONPC} mice was at ages when mortality started to occur, it suggested that the mutant mice died of neurodegenerative brain dysfunction.

Next, we found astrogliosis and microgliosis were markedly elevated in Brap^{cKONPC} cortical tissue in an age-dependent fashion. Increased astrogliosis, identified by Gfap IH and IB analyses, was not detectable in the cerebral cortex Brap^{cKONPC} mice until about 3 months of age. From then, astrogliosis further progressed, becoming fully penetrant and remarkably high as the mutant mice aged rapidly to death (Figure 4C, D; Figure S1A). Parallel to astrogliosis was the strong increase in microgliosis in Brap^{cKONPC} cortices. As the brain's resident innate immune cells, microglia remain in a ramified resting state in healthy brains but can become activated by injury or pathological processes. IH analyses of cortical tissue with pan-microglia marker Iba and activated phagocytic microglia marker CD68 both showed that microglia in Brap^{cKONPC} cortices were de-ramified, amoeboid-like, and activated (Figure 4E). To confirm neuroinflammation, we examined the expression of several key inflammatory molecules implicated in human NDs (Dewachter et al., 2002; Frost et al., 2019; Newcombe et al., 2018; Sarlus and Heneka, 2017) and our RNA-seq data by RT-qPCR. These include C1q, TNFα, TGFβ1, and Trem2, which were all shown to be upregulated significantly in the cortical tissue of 3-month Brap^{cKONPC} mice relative to that of the age-matched WT and/or control mice (Figure 4F). The strong astrocyte and microglial activation along with increased inflammatory cytokines in Brap^{cKONPC} cortical tissue

were consistent with immune activation shown by RNA-seq. These together support the neuroinflammatory and neurodegenerative brain dysfunction of Brap^{cKONPC} mice.

To ascertain Brap LOF leads to neurodegeneration, we examined the brain structure of Brap^{cKONPC} mice that survived to 6 months or older. We first performed a Golgi-Cox stain to reveal the morphology of cortical neurons. While neurons in Brap^{cKONPC} brains were grossly normal in dendritic and axonal morphology, we found that the density of apical dendritic spines was significantly decreased in cortical layer II/III pyramidal neurons of the Brap^{cKONPC} mice compared to those in wild type or control mice, whereas this dendritic spine deficit was very subtle in mutant mice of younger ages (Figure 4G). These results agreed with impaired neuronetwork activities in Brap^{cKONPC} mice revealed by RNA-seq, further supporting an age-dependent decline in cortical neuronal synaptic functions.

To further assess if there was an age-dependent neuronal loss in Brap^{cKONPC} mice, we examined H&E stained brain sections of a set of Brap^{cKONPC} mice (n=8) that survived to 6 months or older. We found all mutant brains showed spongiform encephalopathy in the cortical gray matter (Figure 4H). The spongiform changes were widespread, resulting in striking soma deformation and loss of cortical neurons (Figure 4 I, J; Figure S1B). While spongiform encephalopathy is characteristic for prion diseases, neuronal vacuolization was not associated with the accumulation of the prion protein Prp and was also absent in younger Brap^{cKONPC} mice or control littermates (Figure S1C), indicating it was a non-infectious neuropathological lesion. Many spongiform vacuoles in Brap^{cKONPC} cortices were surrounded by reactive astrocytes and microglia (Figure 4K), suggesting that it was a part of neurodegenerative pathology associated with chronic neuroinflammation.

To ascertain that the neuroinflammatory and neurodegenerative phenotypes of $Brap^{cKONPC}$ mice originate from DSBs in cortical neurons, we tested if neuronal-specific Brap LOF could recapitulate the phenotype of $Brap^{cKONPC}$ mice. For this purpose, we generated and analyzed a Brap neuronal conditional knockout line by abrogating Brap in neurons of the postnatal cortex and hippocampus with a Thy1-Cre driver (Dewachter et al., 2002)($Brap^{flox\ Thy1Cre+;}$ referred to as $Brap^{cKONeuron}$). As expected, about half of the $Brap^{cKONeuron}$ mice (12 out of 21) were found dead by 6 months. Analyses of $Brap^{cKONeuron}$ brains revealed phenotypes indistinguishable from those of the $Brap^{cKONPC}$ mice with respect to increased DSBs, γH2A.X ubiquitination, cellular senescence, tau hyperphosphorylation, astrogliosis, and microgliosis (Figure S1D-I). This demonstrated that the astroglia and microglia activation in $Brap^{cKONPC}$ mice occurred non-cell-autonomously due to defects of cortical neurons. The phenocopy of $Brap^{cKONeuron}$ and $Brap^{cKONPC}$ mice strongly supports the notion that sustained DSBs and senescence-mediated defects in cortical neurons can lead to neuroinflammation, neurodegeneration, and shortened lifespan.

Cellular senescence is associated with histone H2A ubiquitination and histone proteolysis

We next sought to understand the mechanism by which Brap LOF causes cellular senescence. Although DSBs can cause cellular senescence and promote tissue aging, the DDRs that are specifically responsible for inducing the global epigenetic and metabolic changes necessary for reinforcing the senescence state remains unclear. To determine the DDR that drives Brap deficient cells to senescence instead of apoptosis, we looked into the elevation of ubiquityl-γH2A.X, as it is the most distinctive DDR of Brap LOF in both cell cultures and cortical tissues (Figure 2F, K). It is known that mono-ubiquitination of histone H2A and H2A variants, as a

mechanism for chromatin remodeling, can act in a site-specific manner to facilitate transcription silencing and DNA repair, respectively (Uckelmann and Sixma, 2017; Wang et al., 2004). However, Brap LOF increased both mono- and poly-ubiquityl-γH2A.X, which suggested a possibility of ubiquitin-mediated histone degradation. Proteolytic depletion of histones was shown in oncogene-induced senescent human IMR-90 cells (Ivanov et al., 2013), where the autophagy-lysosome pathway (ALP)-dependent histone clearance was found necessary for stabilizing the senescence state. Therefore, we tested if increased γH2A.X ubiquitination may function beyond DNA damage repair and initiate histone clearance. Similar to observations in senescent IMR-90 cells, we found all major histones were progressively depleted as MEFs underwent senescence, while Brap$^{-/-}$ MEFs lost histones more rapidly than the WT MEFs (Figure 5A). This suggested that reducing the total histone content is a common feature of cellular senescence in both human and mouse cells.

Correlated with the histone loss, we observed cytoplasmic histone particles in many Brap$^{-/-}$ MEFs. These cytoplasmic histone particles could be detected by antibodies to all major histones. They were rarely associated with DNA but tightly coincided with reduced nuclear histone abundance and frequently co-occurred with the extrusion of Lamin B1 from the nucleus to the cytoplasm, while the nuclear envelope remained intact (Figure 5B, Figures S2A-C). As Lamin B1's cytoplasmic extrusion and ALP-dependent clearance have also been found to mediate cellular senescence (Dou et al., 2015), we evaluated ALP activities and their contribution to histone degradation in Brap$^{-/-}$ MEFs. We found that the activity of ALP, as indicated by elevated autophagy markers LC3BII and p62/SQSTM1, was significantly stronger in Brap$^{-/-}$ than in WT MEFs (Figure 5C, D). Furthermore, cells showing significant upregulation of p62 and/or LC3B were precisely those that presented a loss of nuclear, but a gain of

cytoplasmic, histones. However, very few cytoplasmic histone particles in Brap$^{-/-}$ MEFs were co-actually localized with p62 and/or LC3B (Figure 5E-G). This raised a possibility that histone clearance in Brap$^{-/-}$ MEFs could be through the ubiquitin proteasome system (UPS) as suggested by the increased polyubiquityl-γH2A.X, while the ALP activation was secondary to increased UPS burden.

To test UPS-dependent histone proteolysis in senescent Brap$^{-/-}$ MEFs, we blocked the activity of UPS by MG132 and re-examined the cytoplasmic histone-p62 or histone-LC3B co-localization. Our data show that MG132 significantly increased the co-localization of cytoplasmic histone particles with p62 or LC3B. In contrast, the lysosome inhibitor chloroquine did not increase cytoplasmic histone-autophagosome co-localization (Figure 5H, I). This indicates that senescent Brap$^{-/-}$ MEFs relied mainly on the UPS for histone clearance.

To verify that the UPS-dependent histone proteolysis was mediated directly by histone ubiquitination, we extracted histones from Brap$^{-/-}$ and WT MEFs and analyzed their UPS- or ALP-dependent ubiquitination state. We found that Brap LOF resulted in a specific increase in both mono- and poly-ubiquitinated histone H2A (mono- or poly-H2Aub). Blocking UPS decreased mono-H2Aub but resulted in marked accumulation of poly-H2Aub, whereas blocking ALP only slightly increased poly-ubiquitinated histones (Figure 5J). These data demonstrate that the UPS is mainly responsible for histone H2A proteolysis in Brap$^{-/-}$ cells, in which mono-H2Aub acts as a primer for poly-H2Aub and UPS targeting. We did not observe changes in ubiquitin-modification of H2B, H3, H4, and H1 (Figure S2D). Although ALP-dependent histone clearance remains possible, UPS targeting of H2Aub is likely the primary underlying mechanism for histone degradation in Brap$^{-/-}$ MEFs. We did not detect altered levels of proteasome 20S core catalytic proteins (Figure 5C, D). However, given the extraordinarily high abundance of histones

in mammalian cells, UPS-dependent histone proteolysis is likely to over-occupy UPS's capacity. Thus, the marked increase in ALP activity in Brap$^{-/-}$ cells may reflect a compensatory response to hijacked UPS, contributing to the clearance of backlogged proteins due to UPS blockage. Consistent with this notion, we observed a remarkable buildup of polyubiquitinated proteins in Brap$^{-/-}$ MEFs as they progressed to senescence (Figure 5K). Therefore, the depletion of histones and the accumulation of a large amount of ubiquitinated cellular proteins in Brap$^{-/-}$ MEFs can together lead to the global epigenetic and metabolic alterations that are necessary for the stable expression of a multitude of phenotypes to reinforce the senescence state.

The hallmark phenotype of Brap LOF is H2Aub mediated by BRCA1 activation

Because H2Aub appeared pivotal for initiating histone proteolysis, we evaluated if it is a primary defect of Brap LOF by examining multiple tissues and ages of Brap mutant mice. As expected, we found H2Aub was significantly elevated in all cells, organs, and ages of Brap$^{-/-}$ and Brap^{cKONPC} mice relative to their wild type and control counterparts (Figure 6A; Figure S3A). Therefore, increases in histone H2Aub is a hallmark phenotype of Brap LOF.

The ubiquitination of histone H2A is mediated by three E3 ligase complexes in a site-specific manner. While the ubiquitin conjugation on K119 is the most prevalent form catalyzed by the polycomb repressive complex 1 (PRC1) (Tamburri et al., 2020), H2A can also be mono-ubiquitinated on K13 and K15 by RNF168/RNF8 or on K125, K127, and K129 by BRCA1 in response to DNA damage (Horn et al., 2019; Kalb et al., 2014; Uckelmann and Sixma, 2017). As IBs with an anti-H2AubK119 antibody only revealed a moderate increase in Brap deficient cells or tissues relative to controls (Figure 5J, Figure 6A, Figure 3SA), H2A is likely

ubiquitinated additionally by RNF168 and/or BRCA1 on residues other than K119 due to persistent DSBs.

Although BRAP resides in the cytoplasm, it can regulate nuclear proteins via two mechanisms: One is to control the nuclear localization of other proteins through importin α, the other is to act as an E3 ligase to regulate other E3 ligases with nuclear targets (Lanctot et al., 2017; Li et al., 1998). It is thus possible that Brap LOF results in H2Aub by altering the nuclear localization or the turnover of E3 ligases that ubiquitinate H2A. Therefore, to determine the contribution of PRC1, Rnf168, and Brca1 to elevated H2Aub caused by Brap LOF, we examined their level and nuclear localization, respectively. Given the close relationship of Brap with Brca1, we first determined if the gained H2Aub in Brap$^{-/-}$ or Brap^{cKONPC} cells and tissues was associated with increased level and activity of Brca1. We found Brca1's abundance in Brap$^{-/-}$ MEFs, NPCs, embryos, as well as postnatal and adult Brap^{cKONPC} cortices was consistently increased in comparison to WT and control cells or cortices (Figure 6B). Besides an overall elevation in total Brca1 protein, our analyses of nuclear and cytoplasmic fractions also showed that the nuclear pool of Brca1 was much higher in Brap$^{-/-}$ than in WT cells (Figure 6C). Moreover, higher levels of nuclear Brca1 was shown in cortical neurons of the Brap^{cKONPC} mice (Figure 6D, Figure S3B). This increased Brca1 abundance and nuclear localization were not only in line with the role of BRAP as BRCA1's cytoplasmic docking protein but also suggested that Brca1 was the DDR- mediator in cells and tissues with Brap LOF. The E3 ligase activity of BRCA1 is integral for BRCA1's role in tumor suppression, though it appears independent of the well-recognized function of BRCA1 in DSB repair (Wu et al., 2009). Besides canonical H2A, the BRCA1 E3 ligase can target several H2A variants, including H2A.X and H2A.Y (MacroH2A1)(Kim et al., 2017). We found H2A.X and H2A.Y were also ubiquitinated at higher

levels in Brap^{cKONPC} than in control mice (Figure 6E, Figure S3C). Taken together, our data suggest strongly that increased Brca1 E3 ligase activity underlies the elevated H2Aub resulting from Brap LOF.

Compared to the robust change in Brca1, alterations in the level and/or nuclear localization of PRC1 and RNF168 by Brap LOF were subtle or undetectable. We also found RNF168 as well as the two main PRC1 molecules, Ring1B and Bmi-1, were abundant in developing cortical tissues but substantially downregulated in adult and aging brains. Consistent with the moderate increase in H2Aub on K119, the levels of Ring1B and Bmi-1 were slightly higher in Brap^{cKONPC} than in control cortices. However, we failed to detect increases in RNF168 in Brap mutants (Figure S3D, E). Collectively, these results suggest that PRC1 and Rnf168 play a stronger role in brain development than in brain aging and that Brca1 is the major downstream partner of Brap in mediating H2Aub, serving as the DDR to drive cells with persistent DSBs to senescence and premature aging.

H2Aub is coupled with impaired proteostasis and neurodegeneration

To determine whether increased histone H2Aub can drive brain aging and promote neurodegeneration, we further examined the histone content, ubiquitinated protein levels, and protein homeostasis in cortical tissues of Brap^{cKONPC} mice. Reminiscent of senescent Brap$^{-/-}$ MEFs, increased mono-H2Aub in Brap^{cKONPC} cortices was accompanied by poly-H2Aub buildup and nuclear histone reductions in a subpopulation of cells (Figure 6F, G). We found cells showing weaker nuclear histone immuno-reactivity were surrounded by reactive astrocytes, supporting the notion that histone proteolysis stabilizes the senescent cell state and mediates the senescence-associated neuroinflammation. Also similar to what was observed in Brap$^{-/-}$ MEFs,

increased mono- and poly-H2Aub was accompanied by substantial elevation of the overall level of poly-ubiquitinated proteins in the Brap^{cKONPC} cortical tissue. While polyubiquitinated proteins in Brap^{cKONPC} cortices were not obviously altered during embryonic and neonatal development, they started to elevate at young adult ages, then further built up progressively with age, and became fully penetrant and remarkably high before Brap^{cKONPC} mice reached their median lifespan of 6 months (Figure 7A, B; Figure S4A, B). The accumulation of a large amount of poly-ubiquitinated proteins, in conjunction with the high level of H2Aub, indicates compromised UPS function. This results in widespread proteopathy in Brap^{cKONPC} cortices, impairing brain functions at multiple levels.

Because the progressive decline in proteostasis is a prominent hallmark of aging and a common pathological feature of neurodegeneration, we assessed the altered cortical proteome in aged cortical tissue of Brap^{cKONPC} mice to evaluate whether it may resemble the proteopathy of NDs. We performed a 10-plex tandem mass tags (TMT) quantitative proteomics analysis of whole cortical proteins from five Brap^{cKONPC} and five control mice of 6 months of age. Out of the total 4708 quantified proteins, the abundance of 903 proteins was significantly altered by Brap LOF, accounting for 19% of total cortical proteins identified by the TMT analysis (Supplemental Table 2). Notably, many toxic proteins associated with Alzheimer's disease (AD), Parkinson's disease (PD), Huntington's disease (HD), and Amyotrophic lateral sclerosis (ALS) were found accumulated in the Brap^{cKONPC} relative to the control cortical tissues (Figure 7C). We further analyzed the global alteration in proteomic profiles resulting from Brap LOF by testing their association with biological processes. In addition to aberrant protein ubiquitination and quality control, Ingenuity Pathway Analysis (IPA) showed that Brap^{cKONPC} cortices also had significantly altered glucose and fatty acid metabolism, deregulated nutrient sensing, as well as a

global decline in numerous cell signaling pathways and neuronal network activities (Figure 7D). Notably, both long-term depression (LTD) and long-term potentiation (LTP) were significantly decreased in Brap^{cKONPC} cortices, indicating diminished synaptic plasticity and impaired cognition of the mutant brain (Figure 7D). These data provided strong evidence for the functional decline of the brain of Brap^{cKONPC} mice before death. While the level of most proteasome 20S catalytic core proteins remains unaltered, we found multiple components of the 19S proteasome regulatory particles were significantly upregulated in Brap^{cKONPC} relative to control cortices (Figure S4C), which suggested increased UPS burden in the mutant. Besides increased ubiquitination of canonical H2A, the abundance of multiple histone H2A variants, including H2A.X, H2A.Y, H2A.Z, H2A.W, and H2A.2B, was also significantly higher in Brap^{cKONPC} than in control cortices (Figure 7E). The changes in H2Aub and multiple histone H2A variants indicate that a broad chromatin remodeling is associated with the age-dependent brain function decline in Brap^{cKONPC} mice, supporting the notion that aging and neurodegeneration can be initiated by global epigenetic alterations mediated by histone H2A and H2A variants.

The overlapping transcriptomic and proteomic alterations between Brap^{cKONPC} mice and NDs prompted us to determine whether the primary defect caused by Brap LOF may underlie human brain aging and neurodegeneration. To establish a link between our findings and NDs, we acquired postmortem brain samples of three Alzheimer's disease (AD) patients along with age-matched normal controls to study their histone levels and histone ubiquitination states (Supplemental Table 3). Intriguingly, our analysis of histone extracts from the human tissue specimen demonstrated that, compared to histone H2A, H2B, H3, or H4, the level of histone H2Aub was overall higher in the cortical tissue of all three AD than in that of control individuals

(Figure 7F; Figure S4D, E). The abundance of mono- and/or poly-H2Aub, albeit variable in different AD individuals and detection conditions, was notably increased in AD relative to control brains. All three AD specimens presented a marked enrichment of the 60 kDa Penta-ubiquitinated H2A (H2Aub5), while increases in H2AubK119 in AD brains were relatively subtle. Moreover, similar to our observations of Brap^{cKO} mice, poly-ubiquitinated histones were found at a higher level in the cortical tissue of AD than in normal age-matched individuals (Figure 7F). The close resemblance in histone ubiquitination between AD and Brap^{cKO} mice suggests that H2Aub is a common epigenetic modification associated with brain aging and neurodegeneration and that the Brap^{cKO} mouse model can serve as a tool for pathogenesis studies of AD and NDs.

DISCUSSION

In this report, we show that Brap LOF causes accelerated aging at the cellular, tissue, and organismal levels, resulting in significant lifespan shortening in mice. This finding is consistent with the results of recent large-scale GWAS that identified the association of *BRAP* locus with human lifespan. They together suggest that a better understanding of *BRAP*'s gain and loss of function would provide insight into the molecular determinants for aging and longevity. Moreover, our studies of the cerebral cortical NPC- and neuron-specific Brap conditional knockout mice reveal a histone H2Aub-based mechanism that connects multiple aging hallmarks to neurodegeneration, serving as a new model for further exploring the pathogenic origin of aging-associated diseases.

The interconnection of multiple aging hallmarks underpins the complex etiology of aging-associated diseases

Aging is an inevitable natural process driven by numerous molecular and cellular events. However, each cellular or molecular event, per se, is insufficient to cause aging-associated morbidity and mortality. At the systemic level, multiple aging promoting mechanisms must act synergistically to cause irreversible functional decline of organs that underpins the complex etiology of aging-associated diseases. BRAP is a multifunctional molecule that connects incoming signals that cells receive to cells' functional outputs governed by chromatin. The E3 ligase activity of BRAP makes it a versatile, yet powerful, molecule to control not only its own levels through auto-ubiquitination but also the level of many cellular proteins through modifying the ubiquitination of other E3 ligases with broad substrates. Therefore, it is not surprising that Brap LOF affects a myriad of cellular proteins and pathways, presenting a multitude of hallmark features of aging including stem cell exhaustion, genome instability, epigenetic alteration, cellular senescence, loss of proteostasis, as well as deregulated nutrient sensing, cell signaling, and cell communication.

Brap LOF has provided us with an excellent model to learn that the abnormal increase in histone H2Aub can serve as a nexus for multiple aging hallmarks. Through studying long-lived Drosophila proteome, a recent study showed that the overall abundance of histone H2A mono-ubiquitination not only increased in aged *Drosophila* but also in an age-dependent manner in the murine heart and brain, as well as in the brain of non-human primate and human (Yang et al., 2019). However, the study attributed such an increase solely to H2AubK119 based on its long life in *Drosophila*, whereas our results partially echo this result by showing a moderate increase of H2AubK119 in Brap mutant mice. Our additional findings demonstrated that the gained

H2Aub in the aging Brap^{cKO} mouse and AD brains was also on residuals other than K119. Moreover, instead of maintaining H2A stability, we show that mono-H2Aub can lead to poly-H2Aub and UPS-mediated histone proteolytic degradation when there are chronic DSBs. This ubiquitin-dependent histone degradation not only results in global epigenetic alteration but also increases the UPS burden, leading to proteopathy and an irreversible senescent state in affected cells.

It is especially intriguing that the overall ubiquitination level of H2A is increased in the cortical tissue of AD. Although the terminal brain pathology of AD is characterized by the accumulation of amyloid-β and hyperphosphorylated tau proteins, the pathogenic origin of AD remains elusive, though aging is known as its major risk factor. Our finding here suggests that histone H2Aub is a potential biomarker for AD, since the level of H2Aub may mark cells' or organs' pathophysiological age instead of chronological age by connecting chromatin aberration to cellular senescence and proteinopathy. While H2Aub-mediated epigenetic and proteomic changes cause profound cell-intrinsic phenotypes, the senescence-associated autocrine and paracrine signaling can result in tissue-wide changes and immune-activation, leading to brain dysfunction at multiple levels. Therefore, epigenetic aging associated with H2Aub may underlie NDs and other aging-associated diseases.

The senescent states are diverse, context-dependent, and can apply to neurons

Cellular senescence, defined traditionally as a cell that can no longer divide, is essentially a stress response to reactive oxygen species, DNA damage, and protein misfolding or aggregation. However, cellular senescence is distinct from cell quiescence by presenting many acquired characteristics beyond cell cycle arrests, such as metabolic activation and SASP. Although Brap^{-}

$^{/-}$ NPCs and MEFs undergo canonical cellular senescence in culture, the senescent phenotype in cortical tissues of Brap^{cKO} mice is more complex. Despite increases in bona fide senescence markers of SA-β-Gal and p16^{Ink4a}, there was no replication arrest of any type of brain-resident cells in the Brap^{cKONPC} brain. Because the age-dependent neuroinflammation, proteopathy, brain structural deterioration, and mid-life mortality were linked to Brap LOF in neurons showing DSBs, it suggests that cellular senescence is dictated by the chromatin state**.** Such chromatin state not only entails the permanent cessation of propagating cells with sustained or irreparable damage but also elicits a multitude of damage responses, leading to the widespread transcriptome, metabolome, and proteome alterations for cells to adjust their microenvironment and their interaction with neighboring cells. Therefore, cellular senescence might be better defined by the distinctive chromatin state, metabolic pattern, and SASP, through which senescent cells can strongly influence multiple cell types in the surrounding tissue. By this definition, neurons, which are already postmitotic, can further progress to a senescent state if they harbor sustained DSBs, leading to brain-wide metabolic and inflammatory changes.

Our RNA-seq with bulk cortical tissue identified 373 upregulated genes in Brap^{cKONPC} mice, of which 80 encode secreted proteins. While some of these transcripts could be from activated astrocytes, microglia, and lymphocytes, many are expected to represent primary SASP of Brap deficient cortical neurons with newly adopted epigenetic states. The molecular responses of cellular senescence are context-dependent. The molecular composition of SASP is expected to be heterogeneous and pleiotropic, which can be both beneficial and destructive depending on the stage of phenotype progression. Further studies to identify primary SASP molecules from Brap deficient cortical neurons in young and aged mice, respectively, will provide in-depth information on the initiation and progression of neuroinflammation and degeneration.

BRCA1-mediated histone H2Aub commits cells to cellular senescence

Brap was originally cloned as a regulator of the BRCA1 tumor suppressor. It binds to the NLS of BRCA1 to control BRCA1's shuttling between the nucleus and the cytoplasm. Variations in BRCA1's nuclear vs. cytoplasmic localization have a strong correlation with aggressive tumor features and/or poor prognosis (Chen et al., 1995; Scully et al., 1996; Wilson et al., 1999). Nonetheless, the role of BRCA1 in tumor suppression is so far attributed to the nuclear pool that directly engages in DNA repair, chromatin remodeling, and transcriptional regulation. The functional significance of cytoplasmic BRCA1 remains unknown. We show that the cytoplasmic pool of Brca1 is decreased upon Brap LOF. The loss of cytoplasmic Brca1 coincides with higher nuclear and overall Brca1 abundance, excessive histone H2Aub, cellular senescence, and accelerated aging. This implicates an anti-senescence and anti-aging role of the cytoplasmic BRCA1. Such function may be especially essential in stem cells and healthy somatic cells, whereas the nuclear BRCA1 pool dominates in cells with genomic lesions. This would well explain the requirement of Brca1 in development as well as the cellular senescence phenotype upon Brca1 abrogation (Cao et al., 2003; Pulvers and Huttner, 2009), though further learning the conditions by which BRAP controls BRCA1's nuclear and cytoplasmic homeostasis is necessary to delineate the diverse roles of BRCA1 in development, aging, and oncogenesis.

Besides a major function in DSB repair, BRCA1 is well recognized by its ubiquitin E3 ligase function. Mutations within the N-terminal RING domain of BRCA1, which abrogates the E3 ligase activity, have been linked to breast and ovarian cancers. The BRCA1 E3 ligase activity was further found independent of its role in DSB repair but essential for tumor suppression (Reid et al., 2008; Wu et al., 2008; Zhu et al., 2011). Data of this study suggest that, by targeting histone H2A for ubiquitination and proteolysis, the BRCA1 E3 ligase mediates an essential DDR

through which it directs cells with chronic DSBs to senescence. Such action can stop the propagation of cells with irreparable DNA damage and prevent their oncogenic transformation. This mechanism can contribute significantly to BRCA1's role in tumor suppression, though it may be at the expense of exhausting stem cells and speeding up the aging of those cells or organs with increased genome instability.

Although Brca1 accounts for the gained histone H2Aub in Brap mutant cells, we do not rule out the possible contribution of other E3 ligases that may function redundantly or synergistically with Brca1 as the H2Aub writer. It is of special note that the histone H2A family contains numerous isoforms and variants. The highest degree of diversification among histone H2A variants is in their C-termini. H2A sits on the edges of the histone octamer with the flexible C-terminus tail protruding from the globular nucleosome particle at the DNA entry/exit site. The structure and variation of the H2A C-termini thus have strong influences on nucleosome stability and chromatin structure. H2Aub produced by BRCA1 was implicated in heterochromatin compaction (Zhu et al., 2011), and chromatin condensation is also the result of histone degradation and replacement by transition proteins in spermatogenesis (Govin et al., 2004). At present, we do not know whether senescence or aging-associated histone proteolysis results in nucleosome-free DNA or histone replacements. Intriguingly, many histone H2A variants were increased in the "aged" Brap^{cKONPC} cortical tissue. This could be due to either compensation for the loss of canonical H2A or an overall change in the turnover of H2A variants. The end result of H2Aub and H2A variants swap could underlie the chromatin response necessary for directing cells with persistent DSBs to senescence as opposed to oncogenesis or apoptosis. Additional insights on the altered nucleosome structure as well as the genomic loci involved in these

chromatin responses will allow a better understanding of the cell fate regulation in response to genomic instability in the brain.

Intrinsic sources of genome instability in cerebral cortical neurons

Studies have shown that DNA damage, particularly DSBs, is elevated in the brains of AD, PD, and ALS patients (Kim et al., 2020; Mitra et al., 2019; Schaser et al., 2019; Shanbhag et al., 2019). While genomic instability is considered a contributor in the pathogenesis of neurodegenerative disorders, the causes of neuronal DSBs and the mechanism by which DSBs drive the degenerative brain pathology remain to be defined. In the cerebral cortical tissue, Brap LOF resulted in chronic DSBs specifically in neurons. While this may be due to neurons' high metabolic rate, potent generation of reactive oxygen species, and abundant polyunsaturated fatty acids prone to peroxidation, we also believe neuronal DSBs are the consequence of aberrant chromatin remodeling in neurogenesis and neuronal maturation during which cortical neurons acquire diversity and the phenotypic plasticity. Although Brap is expressed ubiquitously, in the developing cerebral cortex, Brap LOF impairs specifically the neuronal fate-restrictive cell cycles of NPCs, resulting in hastened G1-phase, abrogation of the G1/S checkpoint, stalled DNA replication, G2 arrest, and decreased neuron production. The aberrant cell cycle kinetics in neuronal differentiation is likely to impair the necessary chromatin modulation required for both the generation and the genome quality control of cortical neurons. Since neurons lack the ability of regeneration, the aberrant chromatin configuration acquired in neuronal differentiation is likely the main source for vulnerability to genotoxic insults throughout neurons' lifespan. We have observed remarkable nuclear architecture aberrations in Brap mutant NPCs and young neurons. These nuclear architecture aberrations mainly involve the constitutive heterochromatin

composed of repetitive satellite DNA sequences (data not shown/manuscript under preparation). It is conceivable that unprotected satellite repeats can increase undesired recombination and DSBs that overwhelm the DNA damage repair machinery. Notably, chromatin immunoprecipitation (ChIP) analyses have shown that mono-H2Aub is enriched in the satellite regions of the genome (Padeken et al., 2019; Zhu et al., 2011). Therefore, the persistently high level of histone H2Aub seen in Brap^{cKO} mice may not only mark the damaged loci but also induce chromatin condensation. Consequently, the broad change in chromatin state can alter gene expression and metabolism to drive neurodegeneration.

The deep chromatin root of neurodegenerative disorders and Alzheimer's disease

Various NDs share common defects in the accumulation and aggregation of misfolded proteins despite the fact that each of them presents unique pathological hallmarks, specific brain regional involvement, and distinctive clinical symptoms. Tremendous effort has been made to target protein aggregates, especially the amyloid plaques in AD, but the efficacy of these treatment regimens has been uncertain, suggesting that the aggregated proteins are the terminally pathological manifestations rather than the original cause of neurodegeneration. It is currently believed that AD, and many other NDs, may have a long asymptomatic phase that lasts as long as decades, during which the diseases are frequently associated with chronic neuroinflammation and brain vascular dysfunction. The complex etiology of NDs has also made it difficult to establish proper animal models. None of the existing models of AD, PD, or ALS fully phenocopies the human disease state and progression. It is thus extremely challenging to identify the early diagnostic markers as well as the initial cellular and molecular defect that primes the progressive brain tissue-wide deterioration.

We believe the Brap^{cKO} mouse model will be invaluable for understanding the molecular mechanism and early-phase pathogenesis of NDs and AD. The wide range of phenotype presented by the Brap^{cKO} mice is well in line with the disease states of human NDs. Its molecular profiles of neuroinflammation as well as gene expression and proteomic aberrations overlap substantially with hallmark pathologies of AD, PD, HD, and ALS. In addition, we have also observed a cerebrovascular phenotype in Brap^{cKO} mice (data not shown). The cerebrovasculature defects, presumably developed from the paracrine effect of SASP following neuronal DSBs, can contribute significantly to the rapid decline of neuronal function. Therefore, data obtained from Brap^{cKO} mice are justified to serve as entry points for exploring the deep roots and complex etiology of neurodegeneration. As suggested, there is a chromatin origin of AD and NDs. Given that dynamic chromatin remodeling is an intrinsic need for neuronal plasticity, genome instability and epigenome aberrations are expected to have a constant and lifelong impact on neuronal function and longevity. A better understanding of chromatin quality control holds promises for the identification of early and effective targets for preventing and treating NDs.

Key Resource Tables:

Supplemental Table 1: RNA-seq Data Table

Supplemental Table 2: TMT Proteomics Data Table

Supplemental Table 3: Human Postmortem AD and Control Brain Tissue Specimen Table

Antibodies Table

Supplemental video

METHODS:

Experimental Model and Subject Details

Mice:

Brap knockout (*Brap*$^{-/-}$), floxed (*Brap*$^{flox/flox}$), and Emx1-cre mediated conditional knockout (*Brap*^{cKONPC}) mice have been described previously (Lanctot et al., 2017). The Thy1-cre mice were purchased from JaxMice (Stock No: 006143) and used to generate *Brap*^{cKONeuron} by crossing with *Brap*$^{flox/flox}$ mice. All mice used for this study were housed and bred according to the guidelines approved by the IACUC committees of Northwestern University and Uniformed Services University of Health Services in compliance with the AAALAC's guidelines. Experiments were performed using littermates or age and genetic background matched control and mutant groups in both sexes. For timed matings, the day of vaginal plug was considered E0.5.

Method Details:

Cell Culture

Neural stem/progenitor cells were isolated from embryonic cortices at E12.5. Single cells were prepared and cultured in DMEM/F12 with N2 and B27 supplements, Penicillin-Streptomycin, Glutamine, Heparin, and growth factors (20 ng/ml EGF and 10 ng/mL FGF). Mouse embryonic fibroblasts (MEFs) were isolated from embryos at E12.5, after removing head and liver. The embryos were minced and digested in 0.25% trypsin-EDTA at 37°C with agitation for 10 min. Single cell suspensions were plated at a density of $\geq 10^4/cm^2$, which is considered passage 0. The cells were then cultured according to the standard 3T3 cell protocol in DMEM supplemented

with 10% FBS and Penicillin-Streptomycin. To block UPS or lysosome, 10 uM MG132, or 25mM chloroquine were applied to MEF culture for 4-12 hours.

Immunoblotting

Immunoblotting of total cell or tissue proteins was performed by extracting with boiling 2x SDS PAGE sample buffer (62.5 mM Tris-HCl, pH 6.8, 2.5% SDS, 0.7135 M β-mercaptoethanol, 10% glycerol, 0.002% Bromophenol Blue) to fully dissolve the tissue proteins, heating at 95°C for 10min to ensure protein denaturation, and passing through syringes with a $29^{1/2}$ gauge needle three times to sheer nuclear DNA and obtain homogenous extracts. 10-30 ug of total proteins were used for each immunoblotting analysis. Loadings were adjusted and normalized by the total protein content according to Coomassie blue stain of the gel after SDS PAGE and by the level of housekeeping proteins.

Immunostaining, Immunofluorescence, and Immunohistological Analyses

Immunofluorescence staining of cells and brain tissue sections was carried out as described (Lanctot et al., 2017; Lanctot et al., 2013). Briefly, cells were fixed with either 4% formaldehyde or cold methanol, blocked in 1% BSA and 5mg/ml lysine, and immuno-stained in a buffer containing 25 mM Hepes, pH 7.4, 250 mM Sucrose, 25 mM KCl, 25 mM $Mg(CH_3COO)_2$, 1% BSA, and 0.25% Saponin. Mouse brains were fixed by transcardial perfusion with PBS and 4% paraformaldehyde and then processed in 12 um cryosections or 5 um paraffin sections. After treating with antigen unmasking solutions (Vector Labs), brain sections were blocked with 5% goat serum and incubated with primary antibodies in PBS, 0.05% Triton X100, and 5% goat

serum at 4°C overnight, and followed by staining with fluorescence conjugated antibodies and Hoechst 33342. Epifluorescence images were acquired with a Leica CTR 5500 fluorescence, DIC, and phase contrast microscope equipped with the Q Imaging Regita 2000R digital camera. Images were imported to Adobe Photoshop and adjusted for brightness and black values.

Senescence-associated β-gal (SA-β-gal) Staining

For identification of cellular senescence, cells were fixed with 2% formaldehyde and 0.2 % glutaraldehyde for 5 min at room temperature. Mouse brains were transcardially perfused and fixed with ice cold PBS followed by 4% paraformaldehyde and 5 mM $MgCl_2$ in PBS for 6-8 hours. The fixed brains were cryopreserved and for prepared as cryosections 16 um in thickness. Fixed cells or brain sections were stained with a staining solution containing 5 mM Potassium Ferrocyanide, 5 mM Potassium Ferricyanide, 150 mM NaCl, 5 mM $MgCl_2$, 40 mM Citric acid-Na phosphate buffer pH 5.95, and 1 mg/ml X-gal at 37°C for 6-20 hours.

Golgi-Cox Staining and Dendritic Spine Analysis

Mice were anesthetized with CO_2; brains were quickly dissected, rinsed with deionized water, immersed in impregnation solution, and processed using FD Rapid GolgiStain kit (FD NeuroTechnologies) according to manufacturer's instructions. Stained sections were examined under a Leica DM5000 light microscope. Pyramidal neurons in the cerebral cortex and hippocampus regions were imaged with 40x objective and photographed. For dendritic spine density analysis, 16-20 pyramidal neurons in neocortical layer II/III of each mouse were randomly selected for assessment. The number of spines per 10 micrometers in secondary apical

dendrites (branched from primary dendrites arising from the soma) was scored using the NIH Image J software.

Histone Extractions

The brain tissues used in this project were provided by the University of California Irvine Alzheimer's Disease Research Center (UCI ADRC) and the Institute for Memory Impairments and Neurological Disorders (UCI MIND). Cell or tissues were re-suspended or homogenized and lysed in PBS containing 0.5% Triton X 100, 25 ug/ml leupeptin, 10 ug/ml Pepstatin A, 5 ug/ml Aprotinin, 10 mM Benzamidine, 2 mM PMSF, 10mM *N*-Ethylmaleimide (NEM), 10mM iodoacetamide (IAA), and 0.02% NaN_3 at a density of ~10^7 cells/ml. Nuclei were first collected by centrifuge at 2500 x g for 10 min at 4°C, washed once, and re-suspend in 0.2 N HCl at a density of $4x10^7$ nuclei per ml to extract histones overnight at 4°C. After clearing debris by centrifugation at 10,000 x g for 10 min at 4°C, the histone containing supernatants were neutralized with 2M Tris Base. Protein concentration was determined by measuring absorbance at 280 nm. Histone extractions were stored in aliquots at -20°C.

Cytoplasmic-nuclear Fractionation

Cells grown on culture dishes were trypsinized, collected in centrifuge tubes with DMEM and 10% FBS, and washed with PBS. After complete removal of PBS, cells were first treated gently with hypotonic buffer (10 mM Hepes, pH 7.9, 1.5 mM $MgCl_2$, and 10 mM KCl) and protease inhibitors on ice for 10 min before the addition of NP-40 to a final concentration of 0.1%. After gently mixing, cells were spun at 2,500 x g for 10 min at 4°C. Supernatants were collected and

analyzed as cytoplasmic fractions either directly or precipitated by 10% TCA. Pellets were gently washed twice with the hypotonic buffer by spinning at 2500 x g for 5 min before being analyzed as nuclear fractions.

RNA Isolation and Quantitative RT-PCR

Cerebral cortical tissue was homogenized in TRIzol reagent (Thermo Fisher) followed by total RNA extraction according to the manufacturer's protocol. 1ug RNA was reverse transcribed into first-strand cDNA using Superscript III reverse transcriptase (Invitrogen). qRT-PCR reactions were performed using Power SYBR Green PCR Master Mix on Roche LightCycler 480 Real-Time PCR system. Primers used for accessing gene expression were synthesized according to validated primer sequences from the MGH-PGA PrimerBank: p16Ink4a (forward: CGCAGGTTCTTGGTCACTGT; reverse: TGTTCACGAAAGCCAGAGCG), Pai-1 (forward: 5'-TTCAGCCCTTGCTTGCCTC; reverse: ACACTTTTACTCCGAAGTCGGT), TGFβ1 (ATGTCACGGTTAGGGGCTC; reverse: GGCTTGCATACTGTGCTGTATAG), Tnf (forward: CTGGATGTCAATCAACAATGGGA; reverse: ACTAGGGTGTGAGTGTTTTCTGT), C1qc (forward: 5'-CCCAGTTGCCAGCCTCAAT-3'; reverse: GGAGTCCATCATGCCCGTC), Trem2 (forward: 5'-CTGGAACCGTCACCATCACTC; reverse: CGAAACTCGATGACTCCTCGG), and Tbp (forward: 5'- AGAACAATCCAGACTAGCAGCA; reverse: GGGAACTTCACATCACAGCTC). Expression was normalized to TATA-binding protein (Tbp) as an internal control and results were analyzed using the $2^{-(\Delta\Delta CT)}$ method.

RNA Sequencing Analysis of Whole Cerebral Cortical Transcriptome

Purified total RNA from whole cerebral cortical tissue of five Brap^{cKONPC} and five control (Brap$^{flox/floxCre-}$ and Brap$^{flox/WTCre-}$) mice at 3 months of age were processed at the University of Chicago Genomics Facility where RNA-seq library preparation was carried out. RNA libraries were sequenced using an Illumina HiSeq 4000 platform (1 x 50 bp single end sequencing). RNA sequencing files were transferred to the Tarbell High-performance computing cluster of Center for Research Informatics at the University of Chicago for analysis. The quality of raw sequencing data was assessed using FastQC v0.11.5. All RNA reads were first mapped to the mouse reference genome (mm10) using STAR v2.5.2b release with default parameters. Picard v2.8.1 (http://broadinstitute.github.io/picard/) was used to collect mapping metrics. Reads were mapped to the mm10 mouse genome assembly. The counted reads were filtered to exclude reads with identical library- and molecule barcodes. Differential gene expression analysis was performed using the DESeq2 package. Significance was defined as FDR corrected p-value < 0.05 and absolute Fold Change ≥ 1.5.

10-plex Tandem Mass Tags (TMT) Proteomic Analysis

Five Brap^{cKONPC} and five control (Brap$^{flox/floxCre-}$ or Brap$^{flox/WTCre-}$) mice at 6 months of age were transcardially perfused with ice cold PBS and protease inhibitors to remove high-abundant blood and serum proteins. Cerebral cortical tissue was dissected on ice, flash frozen in liquid nitrogen, and sent to the Thermo Fisher Center of Harvard Medical School where the samples were processed for 10-plex TMT analysis. MS2 spectra were searched using the SEQUEST algorithm against a Uniprot composite database derived from Mouse proteome containing its reversed complement and known contaminants. Peptide spectral matches were filtered to a 1% false

discovery rate (FDR) using the target-decoy strategy combined with linear discriminant analysis. The proteins were filtered to a <1% FDR. Proteins were quantified only from peptides with a summed SN threshold of >100 and MS2 isolation specificity of 0.5.

Quantification and Statistical Analysis

No statistical methods were used to predetermine sample size, while all experiments were performed with a minimum of three biological replicates and all cell counts were obtained from at least ten random fields. The experiments were not randomized; the investigators were not blinded to the sample allocation and data acquisition during experiments but were blinded in performing quantitative analyses of immunohistological images using the NIH Image J software.

All statistical analyses were done using GraphPad Prism 7.0 software. Data were analyzed by one-way ANOVA or unpaired two-tailed Student's t tests for comparing differences between different genotypes. Differences were considered significant with a p value < 0.05.

ACKNOWLEDGEMENT

The authors wish to thank Barrington Burnett of Uniformed Services University for communication and discussion; the Genomics Facility of University of Chicago for RNA library construction and NGS analysis; the Thermo Fisher Center for Multiplexed Proteomics at the Harvard Medical School for tandem mass tag proteomic analysis; and the Biomedical Instrumentation Center of Uniformed Services University for qRT-PCR analysis. This work was

supported by startup funds of Northwestern University and USUHS to Y.F. The UCI ADRC is funded by NIH/NIA Grant P30AG066519.

AUTHOR CONTRIBUTION

Y.F. conceptualized the project, designed and performed the experiments, interpreted the results, and wrote the manuscript. Y.G. performed experiments; A.A.C. initiated the study and performed the experiments. Y.H. performed data analyses, C.C.L performed experiments, H.P. performed experiments. W-C.C. and J.A. performed bioinformatics data processing and analysis. X.Z. assisted with experiments. E.B. assisted with bioinformatics data analysis. E.S.M. helped with brain pathology data interpretation and the acquisition of the human AD and control brain specimens from the UCI ADRC.

DECLARATION OF INTEREST

The authors declare that they have no conflict of interest.

REFERENCES:

Aoshiba, K., Tsuji, T., Kameyama, S., Itoh, M., Semba, S., Yamaguchi, K., and Nakamura, H. (2013). Senescence-associated secretory phenotype in a mouse model of bleomycin-induced lung injury. Exp Toxicol Pathol *65*, 1053-1062.

Bushman, D.M., Kaeser, G.E., Siddoway, B., Westra, J.W., Rivera, R.R., Rehen, S.K., Yung, Y.C., and Chun, J. (2015). Genomic mosaicism with increased amyloid precursor protein (APP) gene copy number in single neurons from sporadic Alzheimer's disease brains. Elife *4*.

Campisi, J., and Robert, L. (2014). Cell senescence: role in aging and age-related diseases. Interdiscip Top Gerontol *39*, 45-61.

Cao, L., Li, W., Kim, S., Brodie, S.G., and Deng, C.X. (2003). Senescence, aging, and malignant transformation mediated by p53 in mice lacking the Brca1 full-length isoform. Genes Dev *17*, 201-213.

Capparelli, C., Chiavarina, B., Whitaker-Menezes, D., Pestell, T.G., Pestell, R.G., Hulit, J., Ando, S., Howell, A., Martinez-Outschoorn, U.E., Sotgia, F.*, et al.* (2012). CDK inhibitors (p16/p19/p21) induce senescence and autophagy in cancer-associated fibroblasts, "fueling" tumor growth via paracrine interactions, without an increase in neo-angiogenesis. Cell Cycle *11*, 3599-3610.

Castello, L.M., Raineri, D., Salmi, L., Clemente, N., Vaschetto, R., Quaglia, M., Garzaro, M., Gentilli, S., Navalesi, P., Cantaluppi, V.*, et al.* (2017). Osteopontin at the Crossroads of Inflammation and Tumor Progression. Mediators Inflamm *2017*, 4049098.

Chen, Y., Chen, C.F., Riley, D.J., Allred, D.C., Chen, P.L., Von Hoff, D., Osborne, C.K., and Lee, W.H. (1995). Aberrant subcellular localization of BRCA1 in breast cancer. Science *270*, 789-791.

Choy, K.R., and Watters, D.J. (2018). Neurodegeneration in ataxia-telangiectasia: Multiple roles of ATM kinase in cellular homeostasis. Dev Dyn *247*, 33-46.

Coppe, J.P., Desprez, P.Y., Krtolica, A., and Campisi, J. (2010). The senescence-associated secretory phenotype: the dark side of tumor suppression. Annu Rev Pathol *5*, 99-118.

Coppe, J.P., Patil, C.K., Rodier, F., Sun, Y., Munoz, D.P., Goldstein, J., Nelson, P.S., Desprez, P.Y., and Campisi, J. (2008). Senescence-associated secretory phenotypes reveal cell-nonautonomous functions of oncogenic RAS and the p53 tumor suppressor. PLoS Biol *6*, 2853-2868.

Coppede, F., and Migliore, L. (2010). DNA repair in premature aging disorders and neurodegeneration. Curr Aging Sci *3*, 3-19.

d'Adda di Fagagna, F. (2008). Living on a break: cellular senescence as a DNA-damage response. Nat Rev Cancer *8*, 512-522.

Dewachter, I., Reverse, D., Caluwaerts, N., Ris, L., Kuiperi, C., Van den Haute, C., Spittaels, K., Umans, L., Serneels, L., Thiry, E.*, et al.* (2002). Neuronal deficiency of presenilin 1 inhibits amyloid plaque formation and corrects hippocampal long-term potentiation but not a cognitive defect of amyloid precursor protein [V717I] transgenic mice. J Neurosci *22*, 3445-3453.

Dou, Z., Xu, C., Donahue, G., Shimi, T., Pan, J.A., Zhu, J., Ivanov, A., Capell, B.C., Drake, A.M., Shah, P.P.*, et al.* (2015). Autophagy mediates degradation of nuclear lamina. Nature *527*, 105-109.

Flanagan, K.C., Alspach, E., Pazolli, E., Parajuli, S., Ren, Q., Arthur, L.L., Tapia, R., and Stewart, S.A. (2018). c-Myb and C/EBPbeta regulate OPN and other senescence-associated secretory phenotype factors. Oncotarget *9*, 21-36.

Freund, A., Orjalo, A.V., Desprez, P.Y., and Campisi, J. (2010). Inflammatory networks during cellular senescence: causes and consequences. Trends Mol Med *16*, 238-246.

Frost, G.R., Jonas, L.A., and Li, Y.M. (2019). Friend, Foe or Both? Immune Activity in Alzheimer's Disease. Front Aging Neurosci *11*, 337.

Ghosh, K., and Capell, B.C. (2016). The Senescence-Associated Secretory Phenotype: Critical Effector in Skin Cancer and Aging. J Invest Dermatol *136*, 2133-2139.

Gorski, J.A., Talley, T., Qiu, M., Puelles, L., Rubenstein, J.L., and Jones, K.R. (2002). Cortical excitatory neurons and glia, but not GABAergic neurons, are produced in the Emx1-expressing lineage. J Neurosci *22*, 6309-6314.

Govin, J., Caron, C., Lestrat, C., Rousseaux, S., and Khochbin, S. (2004). The role of histones in chromatin remodelling during mammalian spermiogenesis. Eur J Biochem *271*, 3459-3469.

Haber, D.A. (1997). Splicing into senescence: the curious case of p16 and p19ARF. Cell *91*, 555-558.

Hayflick, L. (1965). The Limited in Vitro Lifetime of Human Diploid Cell Strains. Exp Cell Res *37*, 614-636.

Hernandez-Segura, A., Nehme, J., and Demaria, M. (2018). Hallmarks of Cellular Senescence. Trends Cell Biol *28*, 436-453.

Hoang, M.L., Kinde, I., Tomasetti, C., McMahon, K.W., Rosenquist, T.A., Grollman, A.P., Kinzler, K.W., Vogelstein, B., and Papadopoulos, N. (2016). Genome-wide quantification of rare somatic mutations in normal human tissues using massively parallel sequencing. Proc Natl Acad Sci U S A *113*, 9846-9851.

Horn, V., Uckelmann, M., Zhang, H., Eerland, J., Aarsman, I., le Paige, U.B., Davidovich, C., Sixma, T.K., and van Ingen, H. (2019). Structural basis of specific H2A K13/K15 ubiquitination by RNF168. Nat Commun *10*, 1751.

Houlihan, S.L., and Feng, Y. (2014). The scaffold protein Nde1 safeguards the brain genome during S phase of early neural progenitor differentiation. Elife *3*, e03297.

Ivanov, A., Pawlikowski, J., Manoharan, I., van Tuyn, J., Nelson, D.M., Rai, T.S., Shah, P.P., Hewitt, G., Korolchuk, V.I., Passos, J.F.*, et al.* (2013). Lysosome-mediated processing of chromatin in senescence. The Journal of cell biology *202*, 129-143.

Kakigi, R., Endo, C., Neshige, R., Kohno, H., and Kuroda, Y. (1992). Accelerated aging of the brain in Werner's syndrome. Neurology *42*, 922-924.

Kalb, R., Mallery, D.L., Larkin, C., Huang, J.T., and Hiom, K. (2014). BRCA1 is a histone-H2A-specific ubiquitin ligase. Cell reports *8*, 999-1005.

Kim, B.J., Chan, D.W., Jung, S.Y., Chen, Y., Qin, J., and Wang, Y. (2017). The Histone Variant MacroH2A1 Is a BRCA1 Ubiquitin Ligase Substrate. Cell reports *19*, 1758-1766.

Kim, B.W., Jeong, Y.E., Wong, M., and Martin, L.J. (2020). DNA damage accumulates and responses are engaged in human ALS brain and spinal motor neurons and DNA repair is activatable in iPSC-derived motor neurons with SOD1 mutations. Acta Neuropathol Commun *8*, 7.

Kuilman, T., and Peeper, D.S. (2009). Senescence-messaging secretome: SMS-ing cellular stress. Nat Rev Cancer *9*, 81-94.

Lanctot, A.A., Guo, Y., Le, Y., Edens, B.M., Nowakowski, R.S., and Feng, Y. (2017). Loss of Brap Results in Premature G1/S Phase Transition and Impeded Neural Progenitor Differentiation. Cell reports *20*, 1148-1160.

Lanctot, A.A., Peng, C.Y., Pawlisz, A.S., Joksimovic, M., and Feng, Y. (2013). Spatially dependent dynamic MAPK modulation by the Nde1-Lis1-Brap complex patterns mammalian CNS. Dev Cell *25*, 241-255.

Lasry, A., and Ben-Neriah, Y. (2015). Senescence-associated inflammatory responses: aging and cancer perspectives. Trends Immunol *36*, 217-228.

Li, S., Ku, C.Y., Farmer, A.A., Cong, Y.S., Chen, C.F., and Lee, W.H. (1998). Identification of a novel cytoplasmic protein that specifically binds to nuclear localization signal motifs. J Biol Chem *273*, 6183-6189.

Lodato, M.A., Rodin, R.E., Bohrson, C.L., Coulter, M.E., Barton, A.R., Kwon, M., Sherman, M.A., Vitzthum, C.M., Luquette, L.J., Yandava, C.N.*, et al.* (2018). Aging and neurodegeneration are associated with increased mutations in single human neurons. Science *359*, 555-559.

Lodato, M.A., Woodworth, M.B., Lee, S., Evrony, G.D., Mehta, B.K., Karger, A., Lee, S., Chittenden, T.W., D'Gama, A.M., Cai, X.*, et al.* (2015). Somatic mutation in single human neurons tracks developmental and transcriptional history. Science *350*, 94-98.

Lombard, D.B., Chua, K.F., Mostoslavsky, R., Franco, S., Gostissa, M., and Alt, F.W. (2005). DNA repair, genome stability, and aging. Cell *120*, 497-512.

Lopez-Otin, C., Blasco, M.A., Partridge, L., Serrano, M., and Kroemer, G. (2013). The hallmarks of aging. Cell *153*, 1194-1217.

Lu, T., Pan, Y., Kao, S.Y., Li, C., Kohane, I., Chan, J., and Yankner, B.A. (2004). Gene regulation and DNA damage in the ageing human brain. Nature *429*, 883-891.

Luczak, M.W., and Zhitkovich, A. (2018). Monoubiquitinated gamma-H2AX: Abundant product and specific biomarker for non-apoptotic DNA double-strand breaks. Toxicol Appl Pharmacol *355*, 238-246.

Madabhushi, R., Pan, L., and Tsai, L.H. (2014). DNA damage and its links to neurodegeneration. Neuron *83*, 266-282.

Matheny, S.A., Chen, C., Kortum, R.L., Razidlo, G.L., Lewis, R.E., and White, M.A. (2004). Ras regulates assembly of mitogenic signalling complexes through the effector protein IMP. Nature *427*, 256-260.

Mattson, M.P., and Arumugam, T.V. (2018). Hallmarks of Brain Aging: Adaptive and Pathological Modification by Metabolic States. Cell Metab *27*, 1176-1199.

McHugh, D., and Gil, J. (2018). Senescence and aging: Causes, consequences, and therapeutic avenues. The Journal of cell biology *217*, 65-77.

Mitra, J., Guerrero, E.N., Hegde, P.M., Liachko, N.F., Wang, H., Vasquez, V., Gao, J., Pandey, A., Taylor, J.P., Kraemer, B.C.*, et al.* (2019). Motor neuron disease-associated loss of nuclear TDP-43 is linked to DNA double-strand break repair defects. Proc Natl Acad Sci U S A *116*, 4696-4705.

Munoz-Espin, D., and Serrano, M. (2014). Cellular senescence: from physiology to pathology. Nat Rev Mol Cell Biol *15*, 482-496.

Newcombe, E.A., Camats-Perna, J., Silva, M.L., Valmas, N., Huat, T.J., and Medeiros, R. (2018). Inflammation: the link between comorbidities, genetics, and Alzheimer's disease. J Neuroinflammation *15*, 276.

Padeken, J., Zeller, P., Towbin, B., Katic, I., Kalck, V., Methot, S.P., and Gasser, S.M. (2019). Synergistic lethality between BRCA1 and H3K9me2 loss reflects satellite derepression. Genes Dev *33*, 436-451.

Panier, S., and Boulton, S.J. (2014). Double-strand break repair: 53BP1 comes into focus. Nat Rev Mol Cell Biol *15*, 7-18.

Pazolli, E., Alspach, E., Milczarek, A., Prior, J., Piwnica-Worms, D., and Stewart, S.A. (2012). Chromatin remodeling underlies the senescence-associated secretory phenotype of tumor stromal fibroblasts that supports cancer progression. Cancer Res *72*, 2251-2261.

Pulvers, J.N., and Huttner, W.B. (2009). Brca1 is required for embryonic development of the mouse cerebral cortex to normal size by preventing apoptosis of early neural progenitors. Development *136*, 1859-1868.

Quelle, D.E., Zindy, F., Ashmun, R.A., and Sherr, C.J. (1995). Alternative reading frames of the INK4a tumor suppressor gene encode two unrelated proteins capable of inducing cell cycle arrest. Cell *83*, 993-1000.

Rao, S.G., and Jackson, J.G. (2016). SASP: Tumor Suppressor or Promoter? Yes! Trends Cancer *2*, 676-687.

Reid, L.J., Shakya, R., Modi, A.P., Lokshin, M., Cheng, J.T., Jasin, M., Baer, R., and Ludwig, T. (2008). E3 ligase activity of BRCA1 is not essential for mammalian cell viability or homology-directed repair of double-strand DNA breaks. Proc Natl Acad Sci U S A *105*, 20876-20881.

Rodier, F., and Campisi, J. (2011). Four faces of cellular senescence. The Journal of cell biology *192*, 547-556.

Rulten, S.L., and Caldecott, K.W. (2013). DNA strand break repair and neurodegeneration. DNA Repair (Amst) *12*, 558-567.

Rutten, B.P., Schmitz, C., Gerlach, O.H., Oyen, H.M., de Mesquita, E.B., Steinbusch, H.W., and Korr, H. (2007). The aging brain: accumulation of DNA damage or neuron loss? Neurobiol Aging *28*, 91-98.

Salminen, A., Kauppinen, A., and Kaarniranta, K. (2012). Emerging role of NF-kappaB signaling in the induction of senescence-associated secretory phenotype (SASP). Cell Signal *24*, 835-845.

Sarlus, H., and Heneka, M.T. (2017). Microglia in Alzheimer's disease. The Journal of clinical investigation *127*, 3240-3249.

Schaser, A.J., Osterberg, V.R., Dent, S.E., Stackhouse, T.L., Wakeham, C.M., Boutros, S.W., Weston, L.J., Owen, N., Weissman, T.A., Luna, E.*, et al.* (2019). Alpha-synuclein is a DNA binding protein that modulates DNA repair with implications for Lewy body disorders. Scientific reports *9*, 10919.

Scully, R., Ganesan, S., Brown, M., De Caprio, J.A., Cannistra, S.A., Feunteun, J., Schnitt, S., and Livingston, D.M. (1996). Location of BRCA1 in human breast and ovarian cancer cells. Science *272*, 123-126.

Shanbhag, N.M., Evans, M.D., Mao, W., Nana, A.L., Seeley, W.W., Adame, A., Rissman, R.A., Masliah, E., and Mucke, L. (2019). Early neuronal accumulation of DNA double-strand breaks in Alzheimer's disease. Acta Neuropathol Commun *7*, 77.

Soares, J.P., Cortinhas, A., Bento, T., Leitao, J.C., Collins, A.R., Gaivao, I., and Mota, M.P. (2014). Aging and DNA damage in humans: a meta-analysis study. Aging (Albany NY) *6*, 432-439.

Suberbielle, E., Sanchez, P.E., Kravitz, A.V., Wang, X., Ho, K., Eilertson, K., Devidze, N., Kreitzer, A.C., and Mucke, L. (2013). Physiologic brain activity causes DNA double-strand breaks in neurons, with exacerbation by amyloid-beta. Nat Neurosci *16*, 613-621.

Tamburri, S., Lavarone, E., Fernandez-Perez, D., Conway, E., Zanotti, M., Manganaro, D., and Pasini, D. (2020). Histone H2AK119 Mono-Ubiquitination Is Essential for Polycomb-Mediated Transcriptional Repression. Mol Cell *77*, 840-856 e845.

Thadathil, N., Hori, R., Xiao, J., and Khan, M.M. (2019). DNA double-strand breaks: a potential therapeutic target for neurodegenerative diseases. Chromosome Res *27*, 345-364.

Thiriet, C., and Hayes, J.J. (2005). Chromatin in need of a fix: phosphorylation of H2AX connects chromatin to DNA repair. Mol Cell *18*, 617-622.

Timmers, P.R., Mounier, N., Lall, K., Fischer, K., Ning, Z., Feng, X., Bretherick, A.D., Clark, D.W., e, Q.C., Agbessi, M.*, et al.* (2019). Genomics of 1 million parent lifespans implicates novel pathways and common diseases and distinguishes survival chances. Elife *8*.

Todaro, G.J., and Green, H. (1963). Quantitative studies of the growth of mouse embryo cells in culture and their development into established lines. The Journal of cell biology *17*, 299-313.

Uckelmann, M., and Sixma, T.K. (2017). Histone ubiquitination in the DNA damage response. DNA Repair (Amst) *56*, 92-101.

Vaughan, D.E., Rai, R., Khan, S.S., Eren, M., and Ghosh, A.K. (2017). Plasminogen Activator Inhibitor-1 Is a Marker and a Mediator of Senescence. Arterioscler Thromb Vasc Biol *37*, 1446-1452.

Wang, H., Wang, L., Erdjument-Bromage, H., Vidal, M., Tempst, P., Jones, R.S., and Zhang, Y. (2004). Role of histone H2A ubiquitination in Polycomb silencing. Nature *431*, 873-878.

Weidenheim, K.M., Dickson, D.W., and Rapin, I. (2009). Neuropathology of Cockayne syndrome: Evidence for impaired development, premature aging, and neurodegeneration. Mech Ageing Dev *130*, 619-636.

White, R.R., and Vijg, J. (2016). Do DNA Double-Strand Breaks Drive Aging? Mol Cell *63*, 729-738.

Wilson, C.A., Ramos, L., Villasenor, M.R., Anders, K.H., Press, M.F., Clarke, K., Karlan, B., Chen, J.J., Scully, R., Livingston, D.*, et al.* (1999). Localization of human BRCA1 and its loss in high-grade, non-inherited breast carcinomas. Nat Genet *21*, 236-240.

Wu, J., Huen, M.S., Lu, L.Y., Ye, L., Dou, Y., Ljungman, M., Chen, J., and Yu, X. (2009). Histone ubiquitination associates with BRCA1-dependent DNA damage response. Mol Cell Biol *29*, 849-860.

Wu, W., Koike, A., Takeshita, T., and Ohta, T. (2008). The ubiquitin E3 ligase activity of BRCA1 and its biological functions. Cell Div *3*, 1.

Yang, L., Ma, Z., Wang, H., Niu, K., Cao, Y., Sun, L., Geng, Y., Yang, B., Gao, F., Chen, Z.*, et al.* (2019). Ubiquitylome study identifies increased histone 2A ubiquitylation as an evolutionarily conserved aging biomarker. Nat Commun *10*, 2191.

Zhu, Q., Pao, G.M., Huynh, A.M., Suh, H., Tonnu, N., Nederlof, P.M., Gage, F.H., and Verma, I.M. (2011). BRCA1 tumour suppression occurs via heterochromatin-mediated silencing. Nature *477*, 179-184.

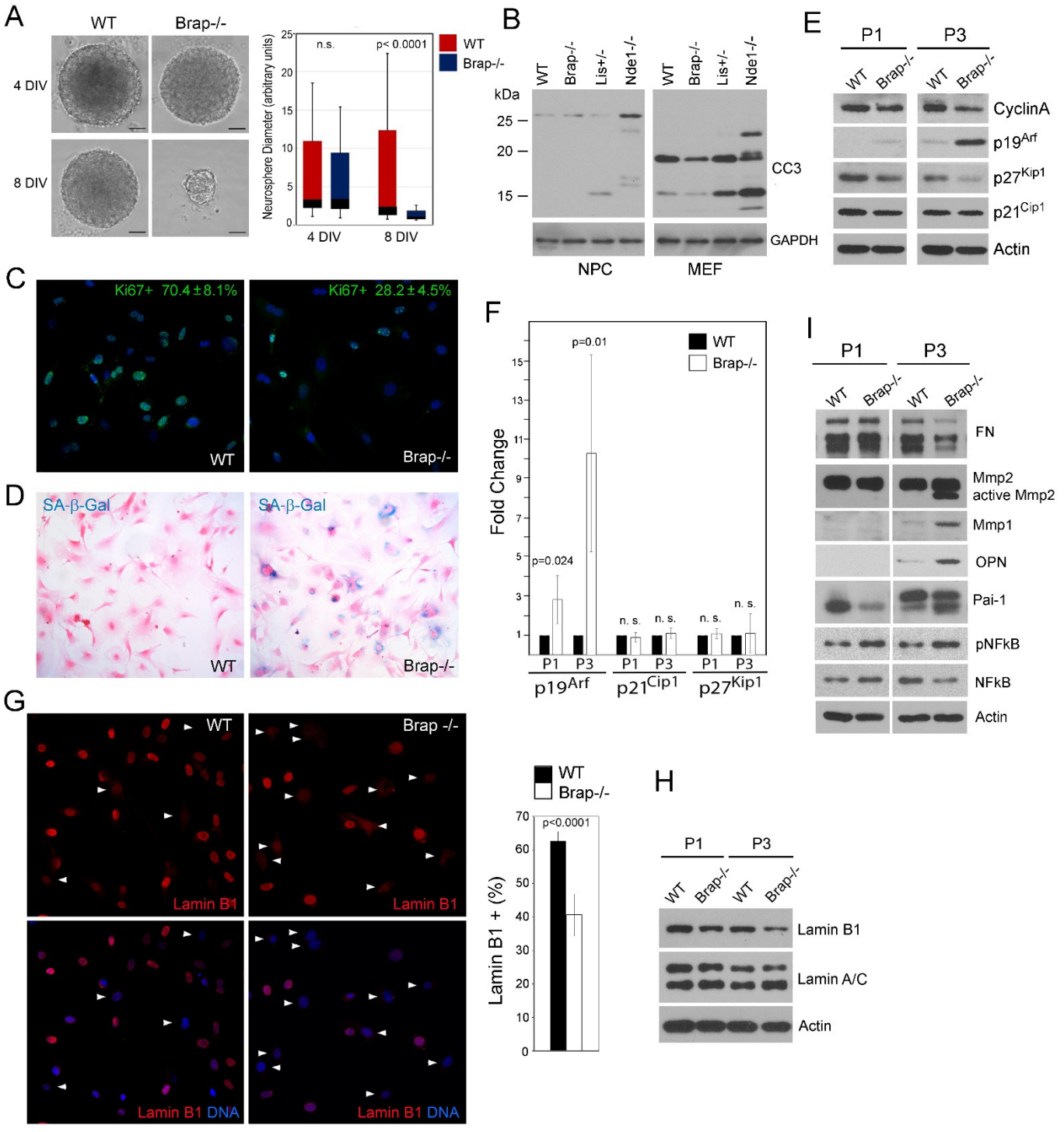

Figure 1. Brap loss of function (LOF) results in accelerated cellular senescence.

A. Primary Brap$^{-/-}$ neural progenitor cells cease growing in culture after 5-7 days in vitro (DIV). Shown are representative images of WT and Brap$^{-/-}$ neurospheres as well as box and whisker plots (Median ± SD) of their diameter distribution at 4 DIV and 8 DIV, respectively.

B. Cleaved caspase 3 (CC3) immunoblotting of total protein extracts of primary neural progenitors and MEFs, respectively. Lis1$^{+/-}$ and Nde1$^{-/-}$ cells were used for CC3 positive control as these cells were known to have levels of apoptosis.

C. Representative Ki67 immunofluorescence images of WT and Brap$^{-/-}$ MEFs at P2. The % of Ki67+ cells (Mean ± SD) is indicated.

D. Senescence-associated β–gal assay of MEFs at P2, which indicates β-galactosidase activity (blue) in higher fraction of Brap$^{-/-}$ cells. Cells were also counter-stained with eosin to view density and cell shape. Note the enlarged cell body of β–gal+ cells.

E, F. Immunoblotting and quantification (Mean ± SD) of G1/S CKIs in total protein extracts from MEFs at P1 and P3, respectively.

G. Representative Lamin B1 immunofluorescence images and percentage (Mean ± SD) of Lamin B1+ MEFs at P2. Cell shown significant reduction of nuclear Lamin B1 are indicated by arrowheads.

H. Immunoblotting of total protein extracts, showing reduced Lamin B1 in Brap$^{-/-}$ relative to WT MEFs at both P1 and P3.

I. Immunoblotting of total protein extracts from MEFs at P1 and P3, showing increased SASP molecules in Brap$^{-/-}$ MEFs at P3. Note the increased Mmps and decreased Mmp substrate fibronection (FN) in Brap$^{-/-}$ MEFs.

Nuclear DNA was stained with Hoechst 33342. Bars: 100 um or as indicated.

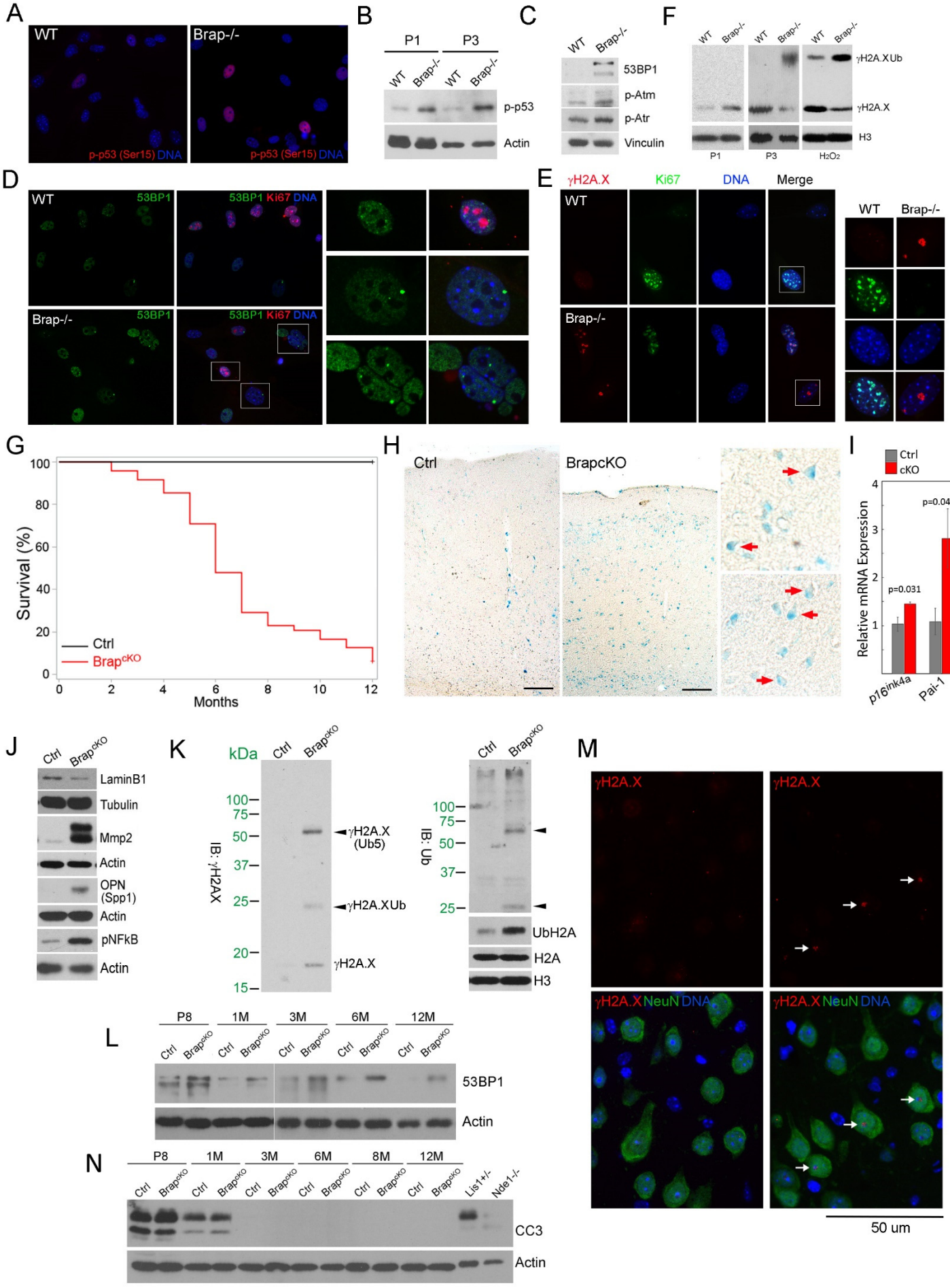

Figure 2. Increased DSBs and DDR are associated with cellular senescence in Brap deficient cells and cerebral cortices.

A. Representative images of phospho-p53 immunofluorescence staining of WT and Brap$^{-/-}$ MEFs at P2.

B. Immunoblotting of total protein extracts from WT and Brap$^{-/-}$ MEFs at P1 and P3, respectively.

C. Immunoblotting of DNA damage response (DDR) proteins in WT and Brap$^{-/-}$ MEFs at P1.

D. Representative images of double immunofluorescence staining of WT and Brap$^{-/-}$ MEFs at P3 with antibodies against Ki67 (red) and 53BP1 (green).

E. Representative images of double immunofluorescence staining of WT and Brap$^{-/-}$ MEFs at P3 with antibodies against Ki67 (green) and γH2A.X (red).

F. Immunoblotting analyses of histone extracts, showing increased γH2A.X and γH2A.X mono-ubiquitination in Brap$^{-/-}$ MEFs.

G. Kaplan-Meier curve shows significantly shortened lifespan of Brap^{cKONPC} mice (n=46) relative to their littermate control mice (n=29).

H. Representative images of senescence-associated β−gal analysis of cerebral cortical sections from Brap^{cKONPC} and control mice at 3 months of age. Note the pyramidal neuronal morphology of some SA-βgal+ cells (red arrows) in high magnification views.

I. qRT-qPCR shows increased expression of p16^{Ink4a} and Pai-1 (plasminogen activator inhibitor-1/Serpine1) in 3-month old Brap^{cKONPC} cortices (Mean ± SD; n=4 biological replicates).

J. Immunoblotting of cerebral cortical total protein extracts, demonstrating higher levels of senescence and SASP-like changes in the cortical tissue of Brap^{cKONPC} relative to littermate control mice.

K. Immunoblotting of histone extracts from cortical tissue of 3-month old Brap^{cKONPC} and control mice, showing elevated γH2A.X as well as the presence of mono- and poly-γH2A.X ubiquitination in Brap^{cKONPC} mice.

L. Immunoblotting of total protein extracts from cortical tissue of Brap^{cKONPC} and control mice, showing persistent elevation of 53BP1 in Brap^{cKONPC} cortices.

M. Representative images of γH2A.X-NeuN double immunohistological staining of cerebral cortical sections from 4-month old WT or Brap^{cKONPC} mice. The presence of γH2A.X immunoreactivity in Brap^{cKONPC} neurons are indicated by arrows.

N. Immunoblotting of total protein extracts from cortical tissue of Brap^{cKONPC} or control mice at various ages, showing that Brap LOF does not increase cleaved caspase 3, an apoptosis marker. Embryonic Lis1$^{+/-}$ and Nde1$^{-/-}$ cortical tissues were used as positive control for the presence of apoptosis.

Nuclear DNA was stained with Hoechst 33342. Bars: 100 um or as indicated.

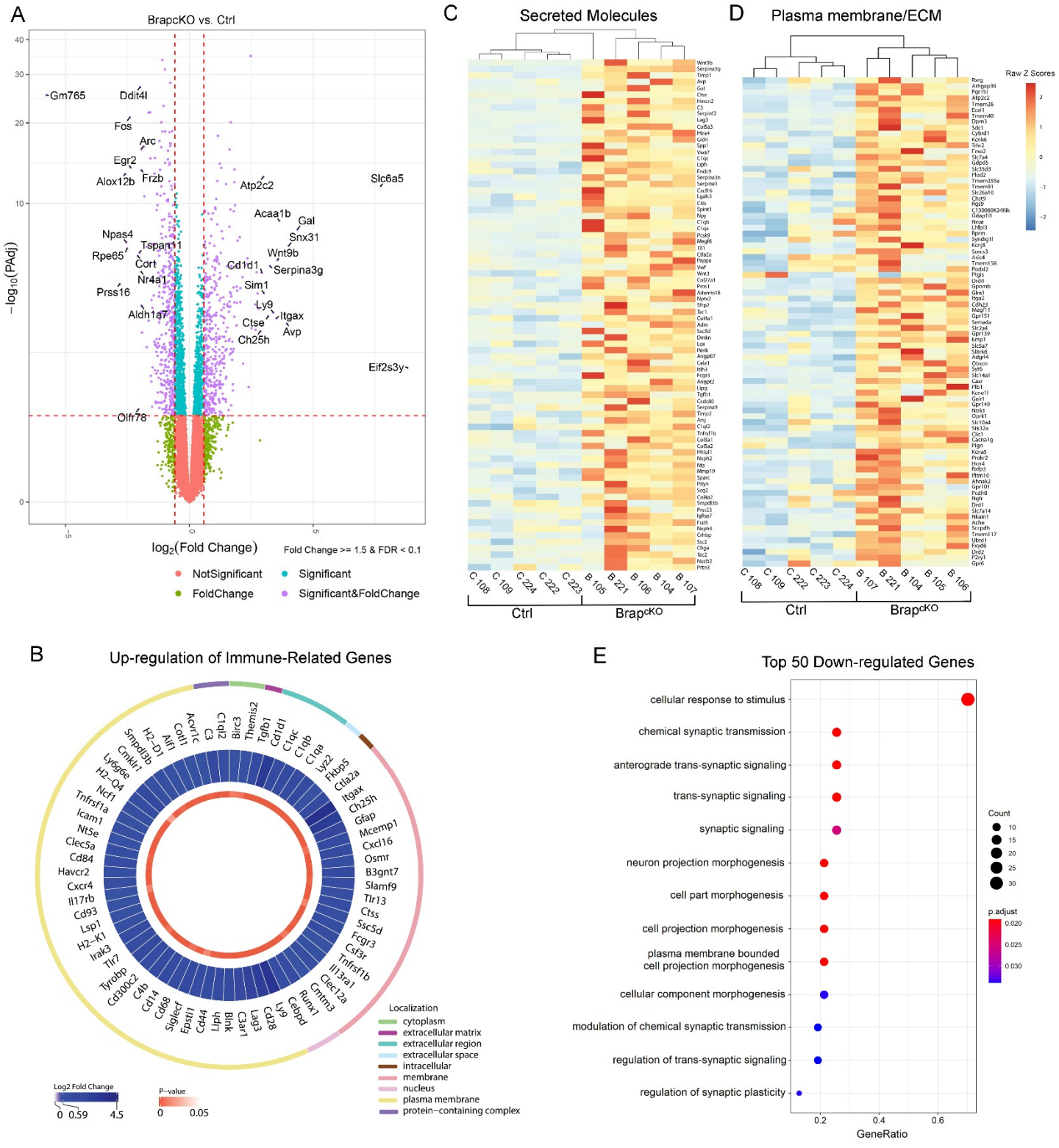

Figure 3. Differential gene expression caused by Brap LOF reveals increased immune activities, SASP profiles, and compromised synaptic function in cerebral cortical tissue.

A. Volcano plot shows differentially expressed genes between Brap^{cKONPC} and control cortical tissues.

B. Circos plot presentation of upregulated genes associated with immune cells and innate immunity regulations in Brap^{cKONPC} relative to control cerebral cortices.

C. Heatmap shows increased expression of genes encoding secreted molecules in Brap^{cKONPC} relative to control cerebral cortices.

D. Heatmap shows increased expression of genes encoding plasma membrane and extracellular matrix molecules in Brap^{cKONPC} relative to control cerebral cortices.

E. GO enrichment analysis of the top 50 down-regulated genes (by adjusted p-value) in Brap^{cKONPC} relative to control cortical tissues. Shown are dot plots of biological processes affected by Brap LOF. Note that synaptic signaling, transmission, and cellular response are significantly compromised in Brap^{cKONPC} cortices.

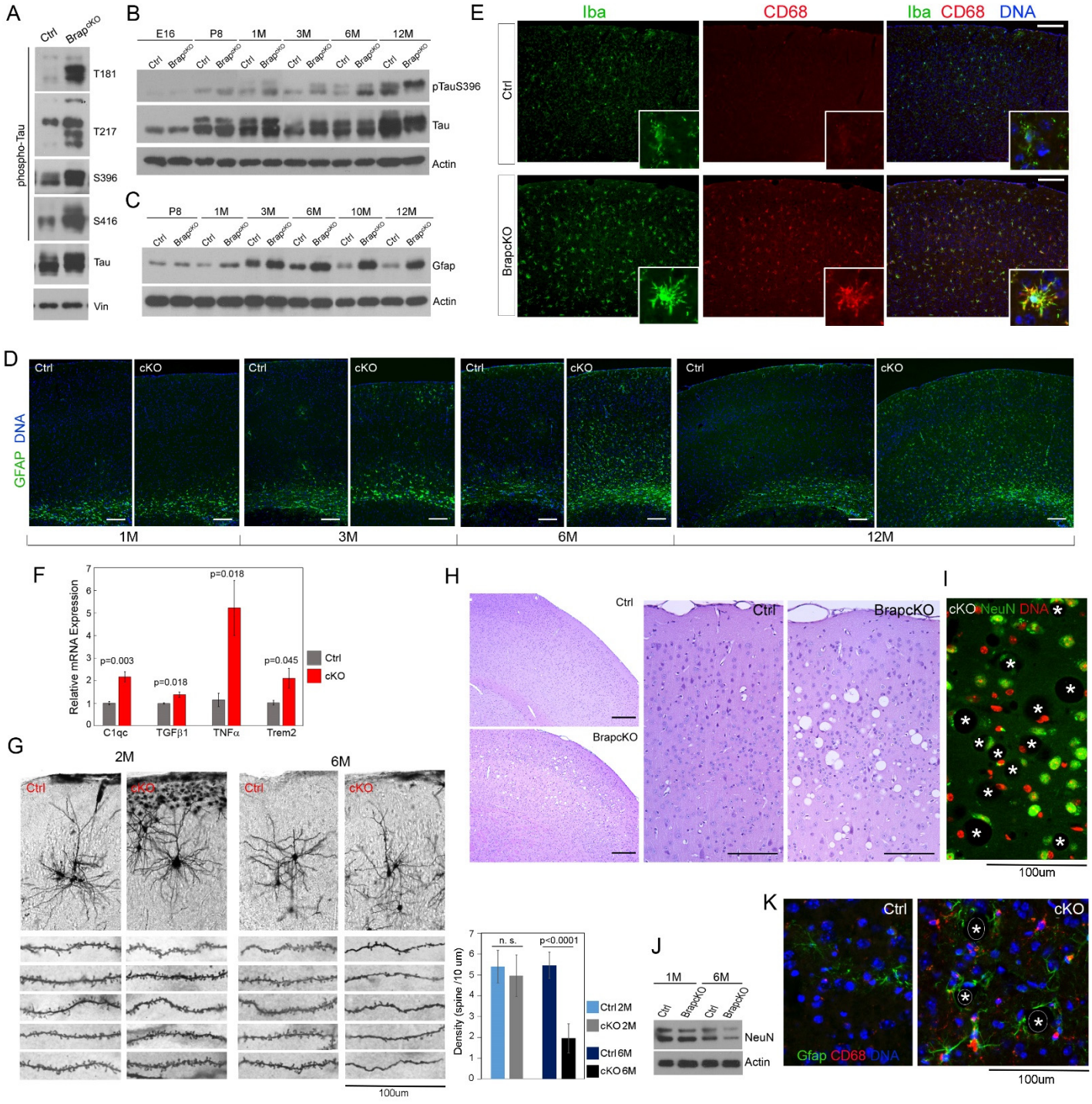

Figure 4. Brap LOF in cerebral cortical NPCs results in neuroinflammation and accelerated neurodegeneration.

A. Immunoblotting of cerebral cortical total protein extracts from 3-month old Brap^{cKONPC} and control mice with various anti-phospho-tau antibodies.

B: Immunoblotting of cortical total proteins extracts shows age-dependent progression of tau hyper-phosphorylation (on S396) in Brap^{cKONPC} cortices.

C, D: Gfap immunohistological and immunoblotting analyses show age-dependent progression of astrogliosis in Brap^{cKONPC} cortices.

E. Double immunohistological staining with anti-Iba (green) and anti-CD68 (red) antibodies shows marked increase in microglia activation in Brap^{cKONPC} cortices at 3 months. Representative images are shown.

F. qRT-PCR analyses of selected neuroinflammatory genes in 3-month cortical tissues (Mean ± SE; n = 4-8 biological replicates).

G. Representative images and quantification (Mean ± SD) of Golgi-cox analyses, showing significantly reduced density of dendritic spine in cortical layer 2/3 pyramidal neurons of Brap^{cKONPC} mice at 6 months.

H. H&E stained brain sections of 10 months old Brap^{cKONPC} and control mice, showing spongiform encephalopathy in Brap^{cKONPC} cortical gray matter.

I. Representative NeuN immunohistological image shows reduced neuronal density and dystrophic or distorted neurons adjacent to spongiosis (positions of vacuoles are marked by asterisks).

J. Immunoblotting of cortical total protein extracts, demonstrating decreased NeuN in Brap^{cKONPC} cortices at 6-month.

K. Representative Gfap (green) and CD68 (red) double immunohistological images, showing increased astrogliosis and microgliosis surrounding the spongiform vacuoles (positions of vacuoles are marked by asterisks).

Nuclear DNA was stained with Hoechst 33342. Bars: 100 um

See also Figure S1.

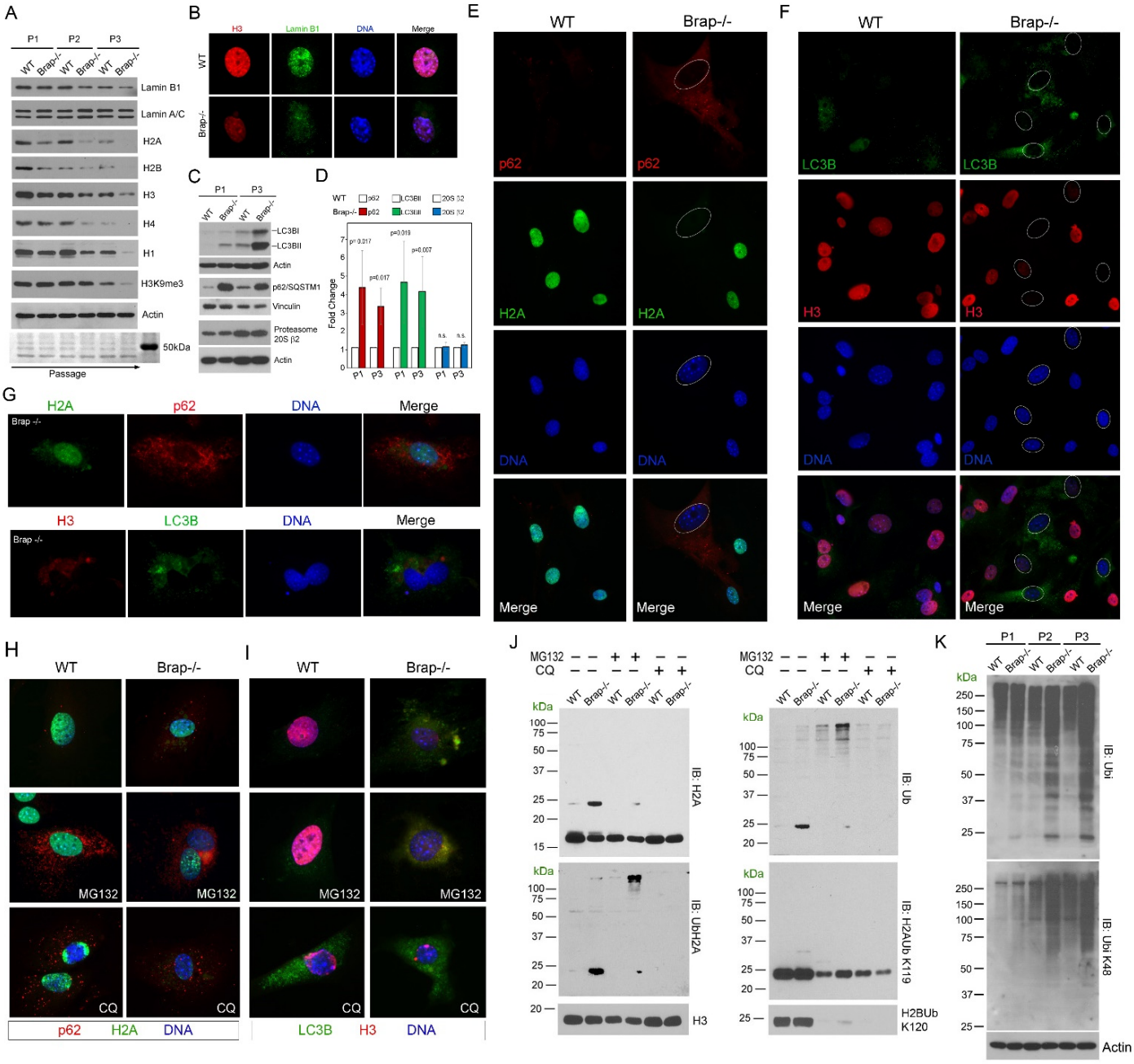

Figure 5. Cellular senescence in Brap$^{-/-}$ MEFs was associated with histone H2A ubiquitination and UPS-mediated proteolysis.

A. Immunoblotting analyses of MEF total protein extracts, showing progressive reduction of Lamin B1 and core histones with increased culture senescence.

B. Representative immunofluorescence image of histone H3 (red) and Lamin B1 (green) double stained MEFs at P3, showing the presence of cytoplasmic Lamin B1 and histone in Brap$^{-/-}$ MEFs.

C. Immunoblotting analyses of autophagy markers LC3B and p62, as well as 20S proteasome catalytic β2 subunit, showing increased autophagy flux without alteration of proteasome abundance in Brap$^{-/-}$ relative to WT MEFs at both P1 and P3.

D. Quantification (Mean ± SD) of p62, LC3BII, and 20Sβ2 levels in WT and Brap$^{-/-}$ MEFs at P1 and P3, respectively. n= 3-5 biological replicates.

E, F, G. Representative immunofluorescence images of WT and Brap$^{-/-}$ MEFs at P3. Antibodies against p62 (red) or LC3B (green) were used to identify autophagosome and co-stained with anti-histone H2A (green) or anti-histone H3 (red). Note that in Brap-/- MEFs, the reduction in nuclear histones coincides with cytoplasmic histone extrusion and correlates with increased autophagy activities but there is little cytoplasmic histone-autophagosome co-localization.

H, I. Representative double immunofluorescence images of MEFs treated with UPS blocker MG132 or lysosome blocker chloroquine (CQ), showing that cytoplasmic H2A-p62 or H3-LC3B co-localization is enhanced by MG132 but not by CQ.

J. Immunoblotting analyses of histone extracts from MEFs at P2, showing Brap LOF caused elevated histone H2A mono- and poly-ubiquitination. The level of poly-H2Aub was further increased by MG132 but not by CQ, indicating UPS-mediated histone H2A proteolysis.

K: Immunoblotting analyses of MEFs total protein extracts, demonstrating increased levels of polyubiquitinated proteins in senescent Brap$^{-/-}$ MEFs.

Nuclear DNA was stained with Hoechst 33342.

See also Figure S2.

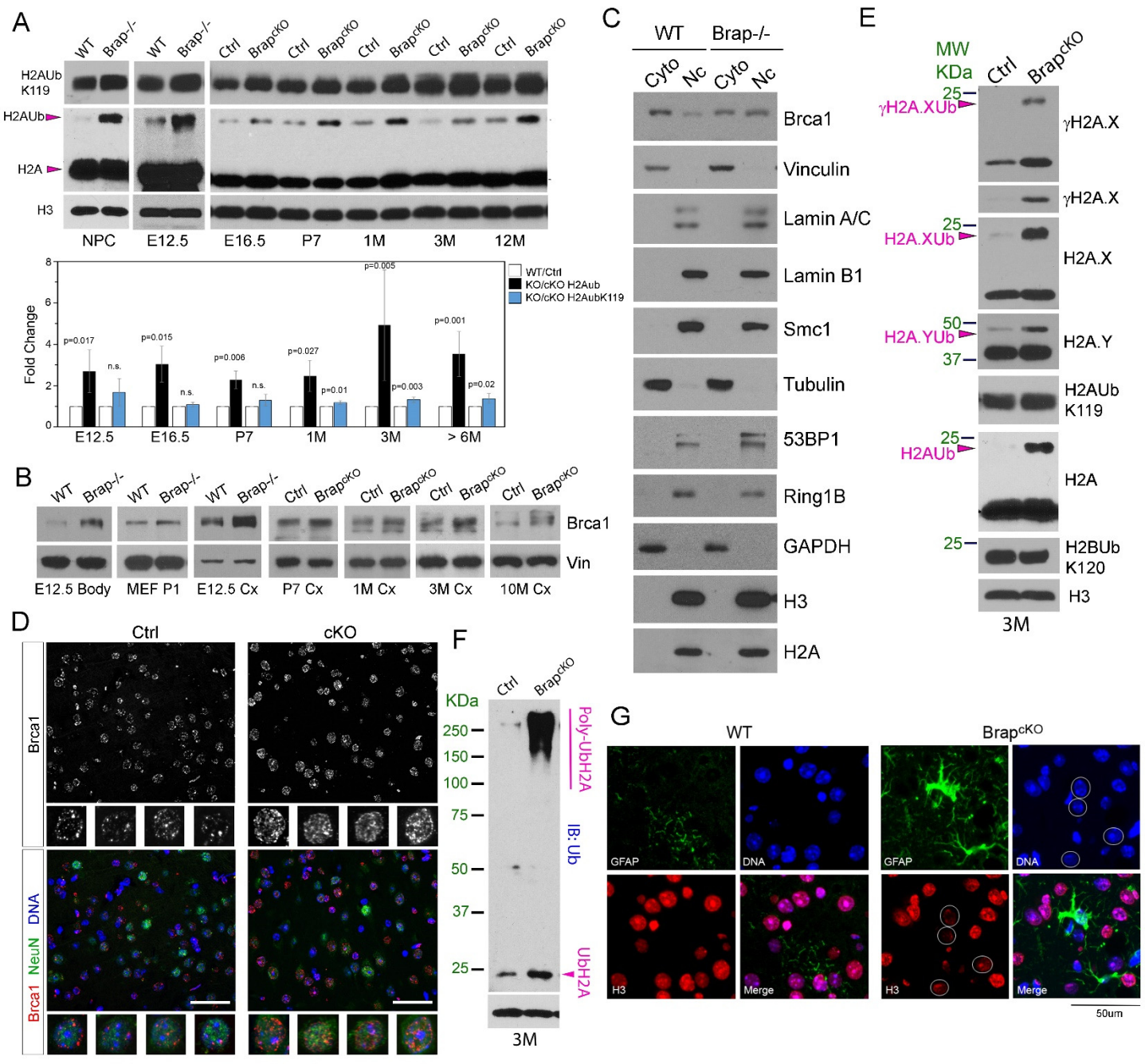

Figure 6. Histone H2A ubiquitination accompanied by Brca1 activation is the hallmark phenotype of Brap LOF

A. Immunoblotting of histone extracts from NPCs as well as from embryonic, neonatal, adult cerebral cortical tissues, and quantification (Mean ± SD) of increases in histone H2Aub (total H2Aub and H2AubK119, respectively) resulted from Brap LOF. n=3-6 biological replicates.

B. Immunoblotting of Brca1 in various cells and tissues, showing that Brap LOF results in increased Brca1 abundance.

C. Immunoblotting of nuclear vs. cytoplasmic fractions of MEFs at P1, showing increased nuclear localization of Brca1 in $Brap^{-/-}$ cells.

D. Brca1 (red) and NeuN (green) double immunohistology images of cerebral cortical sections of $Brap^{cKONPC}$ and control mice at 4 months of age. Representative images are shown. Note the increased intensity and density of Brca1 puncta in the nuclei of $Brap^{cKONPC}$ cortical neurons (NeuN+).

E, F. Immunoblotting analyses of histone extracts from cerebral cortical tissues of 3-month old mice, showing increased ubiquitination of H2A variants targeted by Brca1 (E) along with total histone H2A ubiquitination (F).

G. Double immunohistology staining of cortical sections of 4-month old WT or $Brap^{cKONPC}$ mice with antibodies against Gfap (green) and histone H3 (red), showing reduced nuclear histones in cells surrounded by reactive astrocytes (circles) in $Brap^{cKONPC}$ cortical tissues. Representative images are shown.

Nuclear DNA was stained with Hoechst 33342. Bars: 50 um.

See also Figure S3.

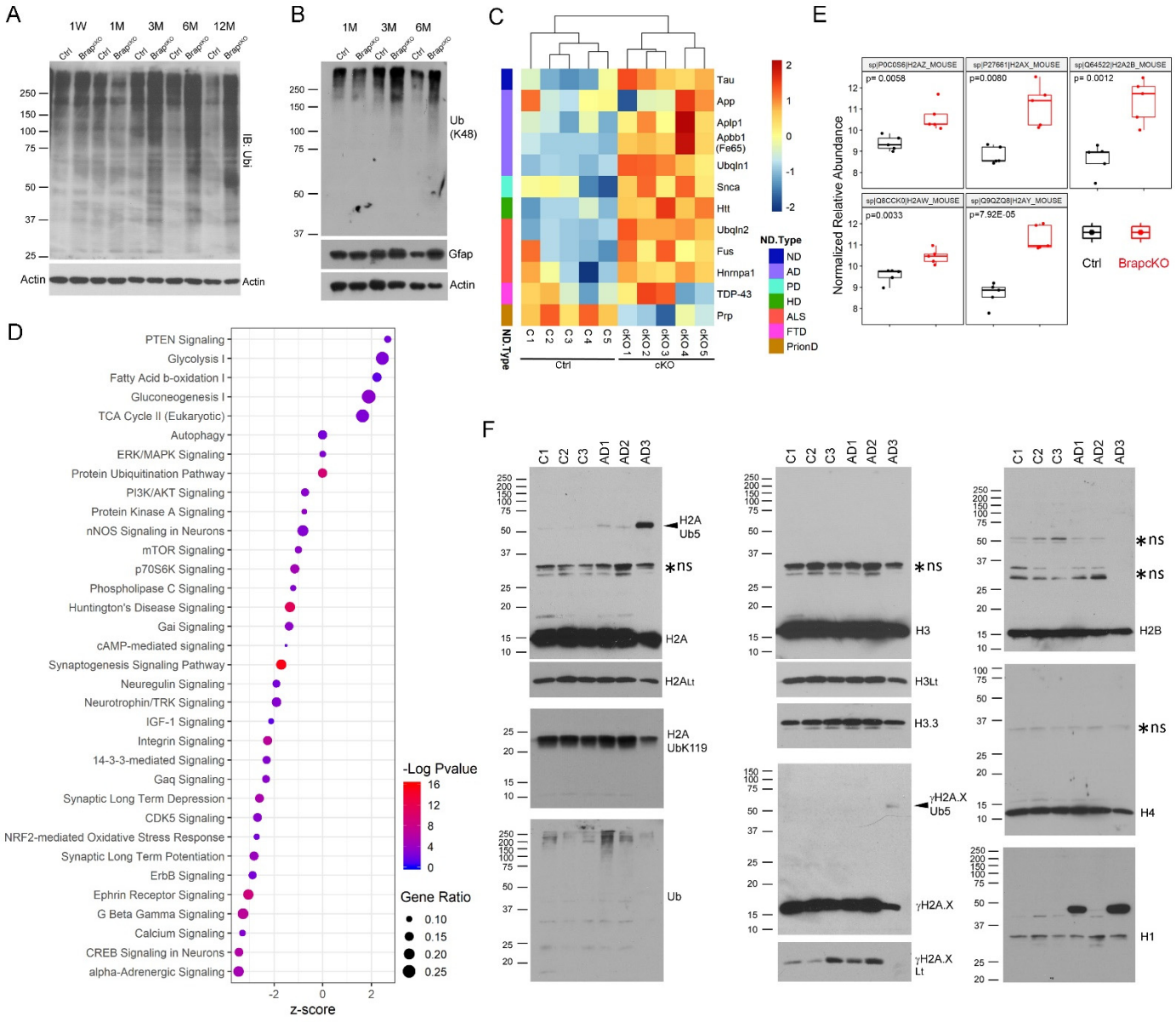

Figure 7. Impaired proteostasis resulted from Brap LOF in cerebral cortical tissue overlaps with proteopathy of neurodegenerative disorders.

A, B. Ubiquitin innunoblots (total ubiquitination or K48-linked polyubiquitination) of cortical tissue total protein extracts from Brap^{cKONPC} and littermate control mice, demonstrating age-dependent accumulation of poly-ubiquitinated proteins in the mutant cortical tissues.

C. Heatmap shows selected proteins accumulated in Brap^{cKONPC} cortical tissue that are also implicated in proteopathy of human neurodegenerative disorders.

D. Dot plot of signaling pathways altered by proteopathy resulted from Brap LOF. Shown were results of IPA of significantly altered proteins revealed by TMT analysis of Brap^{cKONPC} vs. control cortical proteome.

E. Box and whisker plots of selected results of the TMT analysis, showing significant elevation of multiple histone H2A variants in Brap^{cKONPC} relative to control cortical tissues.

F. Immunoblotting of histone extracts from postmortem cortical tissues of AD patients and age matched normal controls, showing significant elevation of H2Aub in AD cortical tissues. Asterisks denote non-specific bands (n.s.).

See also Figure S4.

Supplemental Figure S1

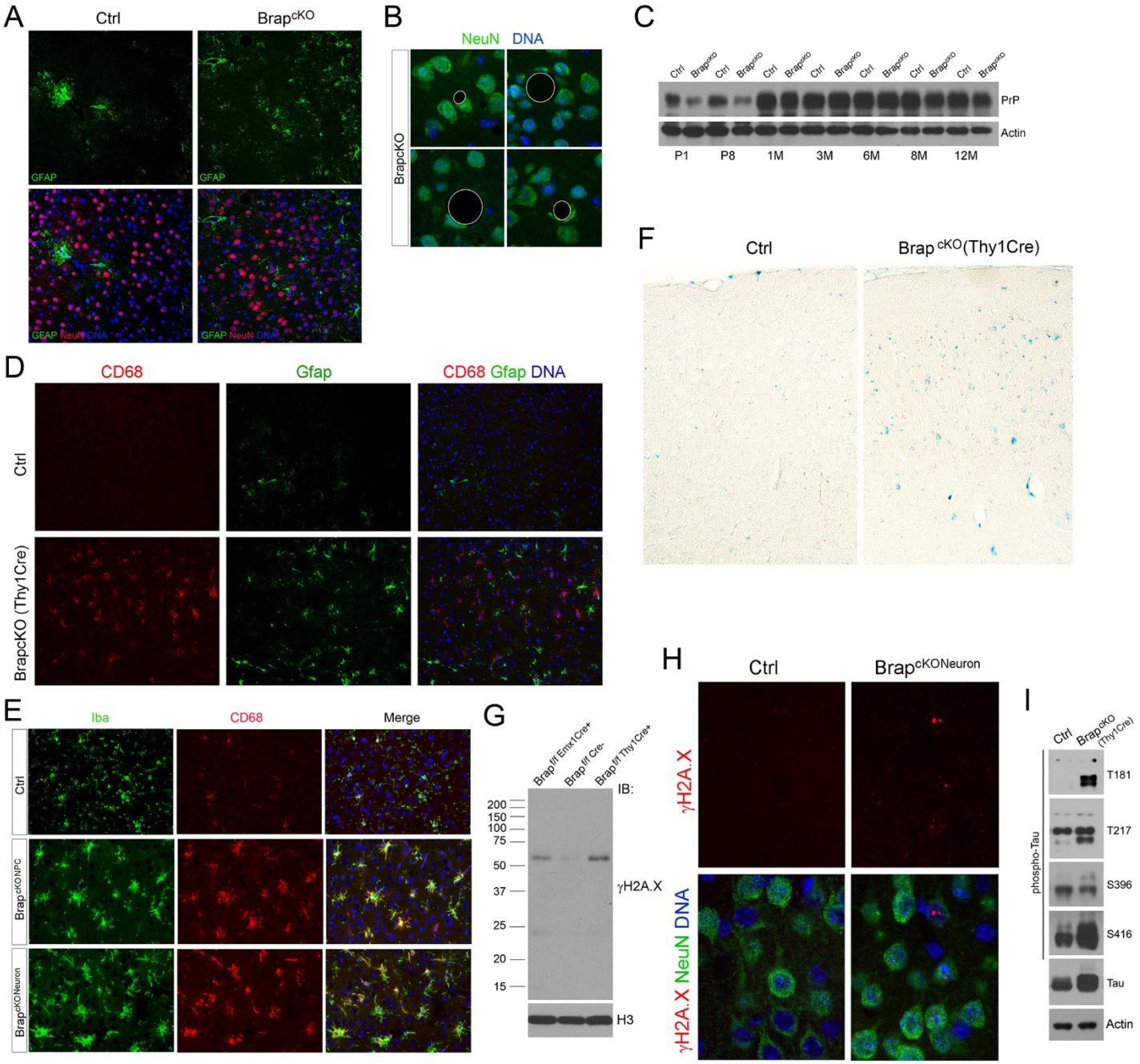

Figure S1 (Related to Figure 4). Phenocopy of Brap^{cKONeuron} with Brap^{cKONPC} mice

A. NeuN (red) and Gfap (green) double immunohistology (IH) staining of cerebral cortical sections of Brap^{cKONPC} and control mice at 6 months of age. Representative images are shown.
B. Representative images of anti-NeuN (green) immunohistological staining of cerebral cortical sections from Brap^{cKONPC} mice at 10 month of age, showing deformed neurons adjacent spongiform vacuoles (marked by circles).
C. Immunoblotting cortical total protein extract with prion protein (Prp) antibodies of Brap^{cKONPC} and control mice at various ages.
D. Representative CD68 (red) and Gfap (green) double immunohistological images, showing microgliosis and astrogliosis in the cortical tissue of Brap^{cKONeuron} mice at 3 months of age.
E. Representative Iba (green) and CD68 (red) double immunohistological images, showing the phenocopy of Brap^{cKONeuron} and Brap^{cKONPC} mice with respect to microglia activation in the cerebral cortical tissue at 3 months of age.
F. Senescence-associated β−gal analysis of cerebral cortices of Brap^{cKONeuron} and control mice at 3 months of age. Representative images are shown.
G. Immunoblotting of cerebral cortical histone extracts, showing the phenocopy of Brap^{cKONeuron} and Brap^{cKONPC} mice with respect to the elevation of ubiquityl- γH2A.X.
H. NeuN (green) and γH2A.X (red) double immunohistological images of cortical section of Brap^{cKONeuron} and control mice at 3 months of age, showing the presence of neuronal-specific DSBs in Brap^{cKONeuron} mice.
I. Immunoblotting of cerebral cortical total protein extracts of 3-month old Brap^{cKONeuron} and control mice with anti-phospho-tau antibodies, showing tau hyper-phosphorylation on multiple residues in mutant cortices.

Nuclear DNA was stained with Hoechst 33342.

Supplemental Figure S2

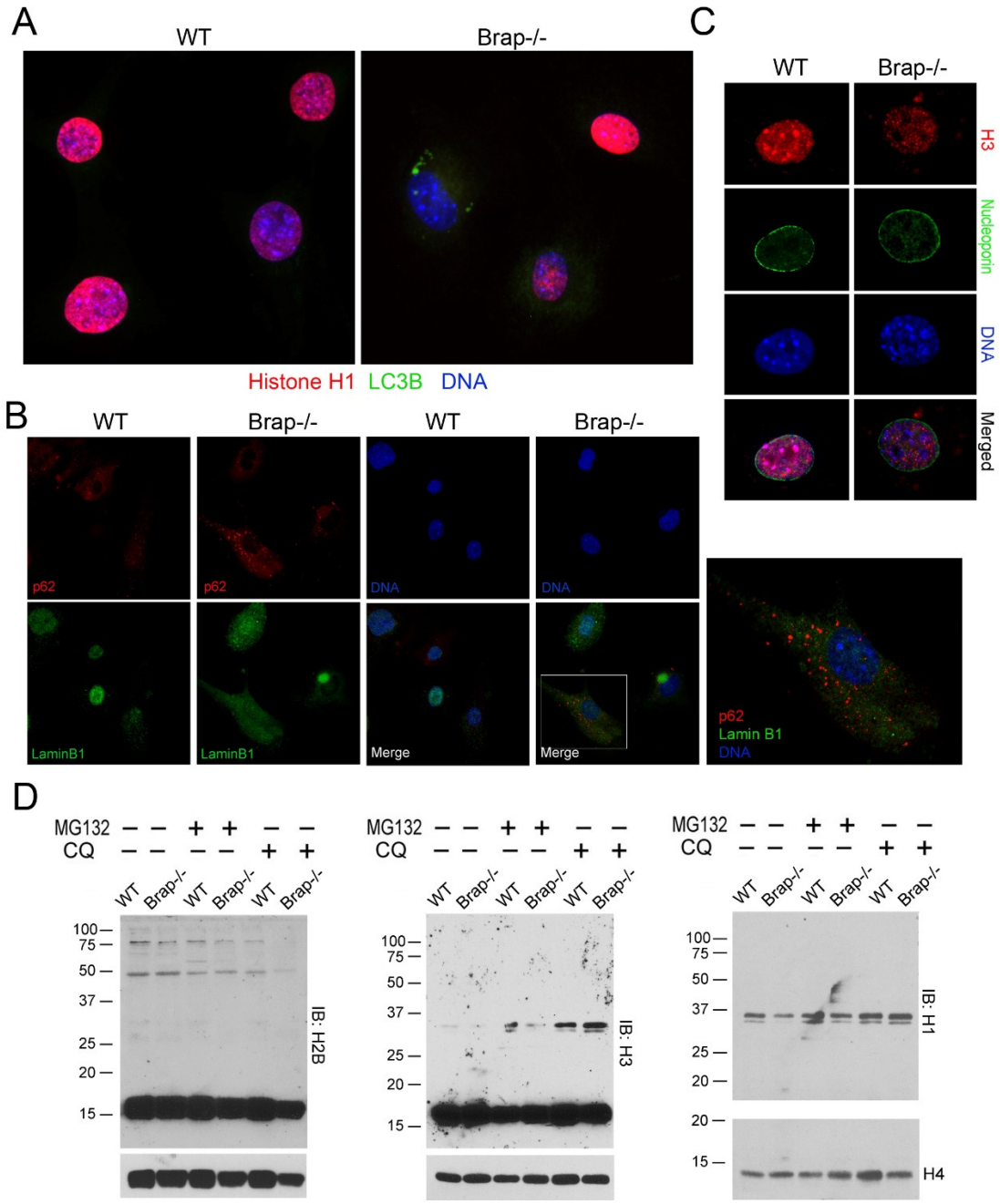

Figure S2 (Related to Figure 5). Brap LOF results in loss of nuclear histones and nuclear Lamin B1.
A. Immunofluorescence images of WT and Brap$^{-/-}$ MEFs at P3 stained with antibodies to histone H1 and anti-LC3B, showing the correlation of reduced histone H1 with increased cytoplasmic LC3B.
B. Immunofluorescence images of WT and Brap$^{-/-}$ MEFs at P3 stained with antibodies against Lamin B1 and p62, showing the correlation of reduced nuclear Lamin B1 with increased cytoplasmic Lamin B1 and p62.
C. Immunofluorescence images of WT and Brap$^{-/-}$ MEFs at P3 stained with anti-nuceloporin and histone H3, showing intact nuclear envelope despite the presence of cytoplasmic histone H3 in Brap$^{-/-}$ MEFs.
D. Immunoblotting analyses of histone extracts from MEFs at P2, showing that the ubiquitination of histone H2B, H3, H4, and H1 was not obviously altered by Brap LOF.

Supplemental Figure S3

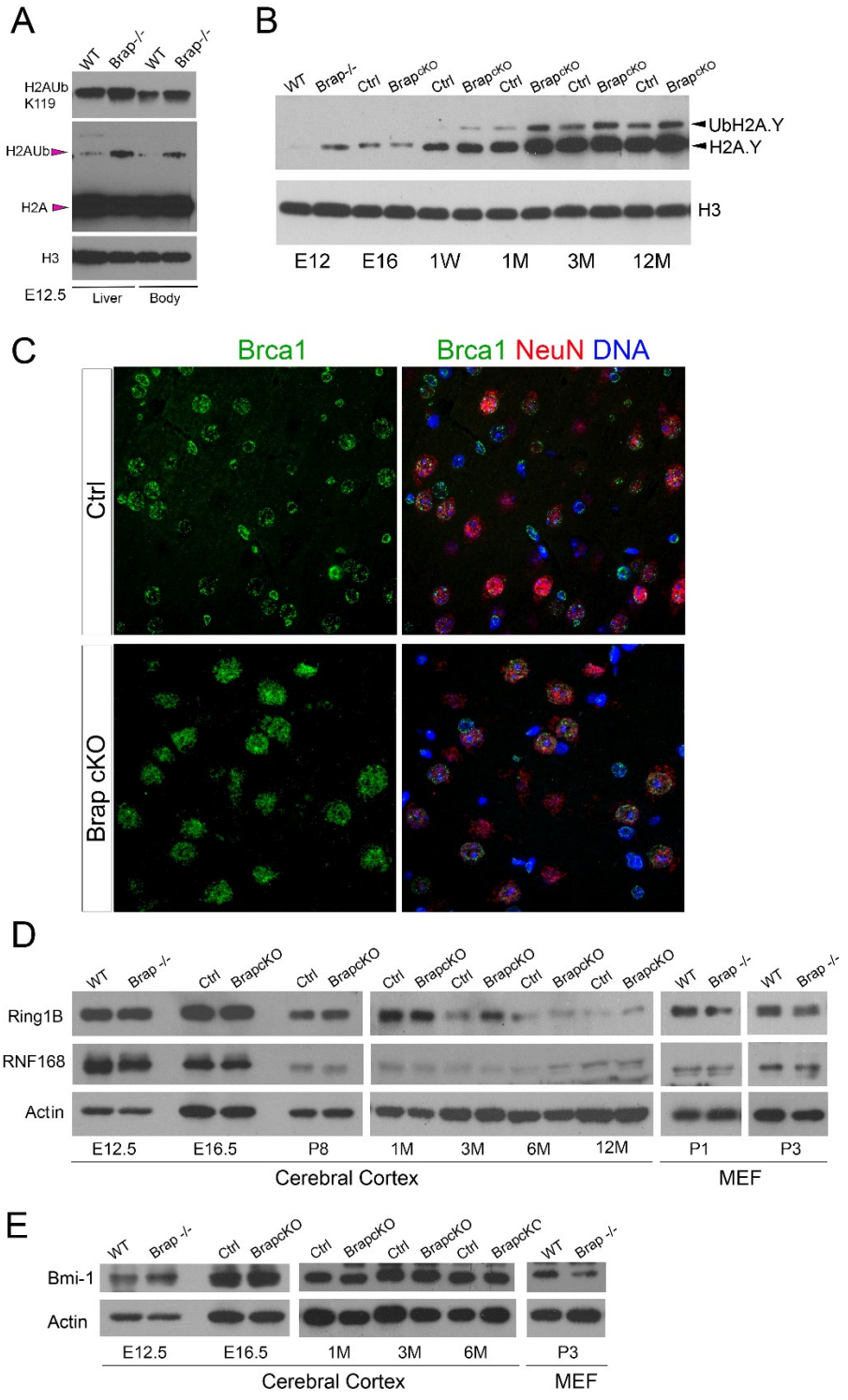

Figure S3 (Related to Figure 6). Brap LOF increases histone H2Aub along with ubiquityl-H2A.Y targeted by Brca1 E3 ligase.

A. Immunoblotting of histone extracts from embryonic liver and body tissues, showing higher level of H2Aub in Brap$^{-/-}$ than in of WT mice.

B. Immunoblotting of histone extracts from cerebral cortical tissue at various ages, showing increased H2A.Y (MacroH2A) ubiquitination in postnatal, adult, and aged Brap^{cKONPC} mice.

C. Brca1 (red) and NeuN (green) double immunohistology images of cerebral cortical sections of Brap^{cKONPC} and control mice at 1 month of age. Representative images are shown.

D, E Immunoblotting of total protein extracts from cortical tissues or MEFs from WT, Brap$^{-/-}$, Brap^{cKONPC}, and control mice at various ages.

Supplemental Figure S4

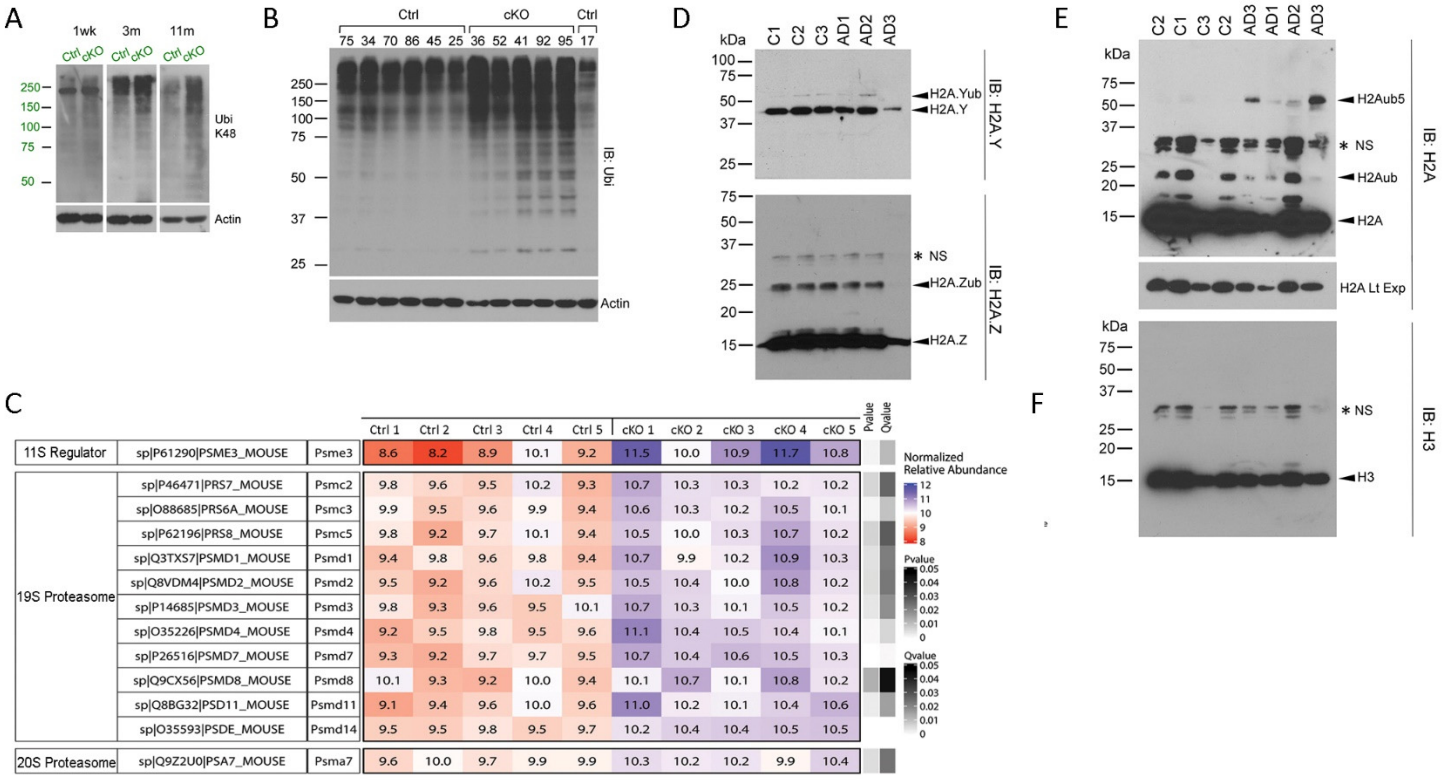

Figure S4 (Related to Figure 7). Accelerated brain aging of Brapc^{KONPC} mice is associated with accumulation of poly-ubiquitinated proteins in cerebral cortical tissue and shared increase in H2Aub between Brapc^{KONPC} mice and AD patients.

A. Immunoblotting of cerebral cortical total protein extracts, showing age-dependent increase in K48-linked polyubiquitinated protein destined to UPS degradation in Brap^{cKONPC} cortices.

B. Anti-ubiquitin immunoblotting of total protein extracts from Brap^{cKONPC} and control mice at 6 months of age, showing the phenotype is fully penetrant.

C. Table and heatmap show the significant accumulation of proteasome catalytic and regulatory proteins in Brap^{cKONPC} cortical tissue revealed by TMT analysis.

D. Immunoblotting AD postmortem cortical tissue histone extracts with antibodies against histone H2A.Y and H2A.Z, respectively. Asterisks denote non-specific bands.

E. Immunoblotting AD postmortem cortical tissue histone extracts with antibodies against histone H2A. This represents a technical replication of Figure 7F. Asterisks denote non-specific bands.

Graphic Abstract